Empirical–Statistical Downscaling of Austral Summer Precipitation over South America, with a Focus on the Central Peruvian Andes and the Equatorial Amazon Basin

JUAN SULCA,[a] MATHIAS VUILLE,[b] OLIVER ELISON TIMM,[b] BO DONG,[c] AND RICARDO ZUBIETA[a]

[a] *Instituto Geofísico del Perú, Lima, Peru*
[b] *Department of Atmospheric and Environmental Sciences, University at Albany, State University of New York, Albany, New York*
[c] *Department of Meteorology, University of Reading, Reading, United Kingdom*

(Manuscript received 17 March 2020, in final form 29 September 2020)

ABSTRACT: Precipitation is one of the most difficult variables to estimate using large-scale predictors. Over South America (SA), this task is even more challenging, given the complex topography of the Andes. Empirical–statistical downscaling (ESD) models can be used for this purpose, but such models, applicable for all of SA, have not yet been developed. To address this issue, we construct an ESD model using multiple-linear-regression techniques for the period 1982–2016 that is based on large-scale circulation indices representing tropical Pacific Ocean, Atlantic Ocean, and South American climate variability, to estimate austral summer [December–February (DJF)] precipitation over SA. Statistical analyses show that the ESD model can reproduce observed precipitation anomalies over the tropical Andes (Ecuador, Colombia, Peru, and Bolivia), the eastern equatorial Amazon basin, and the central part of the western Argentinian Andes. On a smaller scale, the ESD model also shows good results over the Western Cordillera of the Peruvian Andes. The ESD model reproduces anomalously dry conditions over the eastern equatorial Amazon and the wet conditions over southeastern South America (SESA) during the three extreme El Niños: 1982/83, 1997/98, and 2015/16. However, it overestimates the observed intensities over SESA. For the central Peruvian Andes as a case study, results further show that the ESD model can correctly reproduce DJF precipitation anomalies over the entire Mantaro basin during the three extreme El Niño episodes. Moreover, multiple experiments with varying predictor combinations of the ESD model corroborate the hypothesis that the interaction between the South Atlantic convergence zone and the equatorial Atlantic Ocean provoked the Amazon drought in 2015/16.

KEYWORDS: Atlantic Ocean; Intertropical convergence zone; South America; South Atlantic convergence zone; Tropics; ENSO; Teleconnections; Precipitation; Summer/warm season

1. Introduction

The three extreme episodes of El Niño in 1982/83, 1997/98 and 2015/16 caused different types of impacts in South America, such as drought over the equatorial Amazon basin (Jiménez-Muñoz et al. 2016) and floods over southeastern South America (Emerton et al. 2017). In Peru, the extreme El Niños of 1982/83 and 1997/98 led to significant losses to the Peruvian economy as a consequence of floods and droughts [as documented by the Peruvian National Service of Meteorology and Hydrology (SENAMHI) and others; SENAMHI 2014; Huggel et al. 2015; Rodríguez-Morata et al. 2018] and El Niño of 2015/16 caused relatively minor impacts (French and Mechler 2017). SENAMHI (2014) documented that El Niño 1982/83 caused precipitation totals near 3000 mm from September to May on the northern coast of Peru (around 2000% of their climatological mean), while a severe deficit of precipitation characterized the southern Andes. During El Niño 1997/98, the northern coast of Peru again recorded precipitation totals near 3000 mm from September to May, with maximum precipitation in Piura and Tumbes, while the southern Andes registered a deficit of precipitation but weaker than during El Niño 1982/83. According to Vargas (2009), Peru registered economic losses around $3283 million and $3500 million (U.S. dollars) during El Niños of 1982/83 and 1997/98, respectively. El Niño 2015/16 caused several disasters, but their intensities were weaker than during El Niños 1982/83 and 1997/98 because the warm SST anomalies were restricted to the central equatorial Pacific Ocean (L'Heureux et al. 2016). SENAMHI (2019) documented that the drought covered around 25% of the area in 4 of 24 Departments of Peru (Apurímac, Cusco, Huancavelica, and Puno). Economically, the Peruvian Council of Risk Management for the phenomenon El Niño requested disbursement of around $206 million (U.S. dollars) to address the impacts of the El Niño 2015/16.

One of the main goals of this study is to provide a framework that would allow for a better estimation and prediction of precipitation in South America and in particular over Peru, with a special emphasis on one of Peru's key agricultural areas that is significantly affected by extreme weather, the Mantaro basin (MB). This basin is located within the central Andes of Peru (10°34′–13°35′S, 73°55′–76°40′W) (Fig. 1) and covers approximately 34 550 km^2, over an elevation range from 500 to 5350 m MSL. The wet period in the MB occurs between September and April of the following year, with the maximum precipitation falling during austral summer [December–February (DJF)]. The DJF precipitation is associated with an enhanced upper-level easterly flow over the MB. In contrast, the dry season in the MB occurs during episodes of anomalous upper-level westerly flow over the central Andes of Peru (Instituto Geofísico del Peru 2005). Years with below-average DJF precipitation can lead to negative impacts in the MB, related

Corresponding author: Juan Sulca, sulcaf5@gmail.com

DOI: 10.1175/JAMC-D-20-0066.1

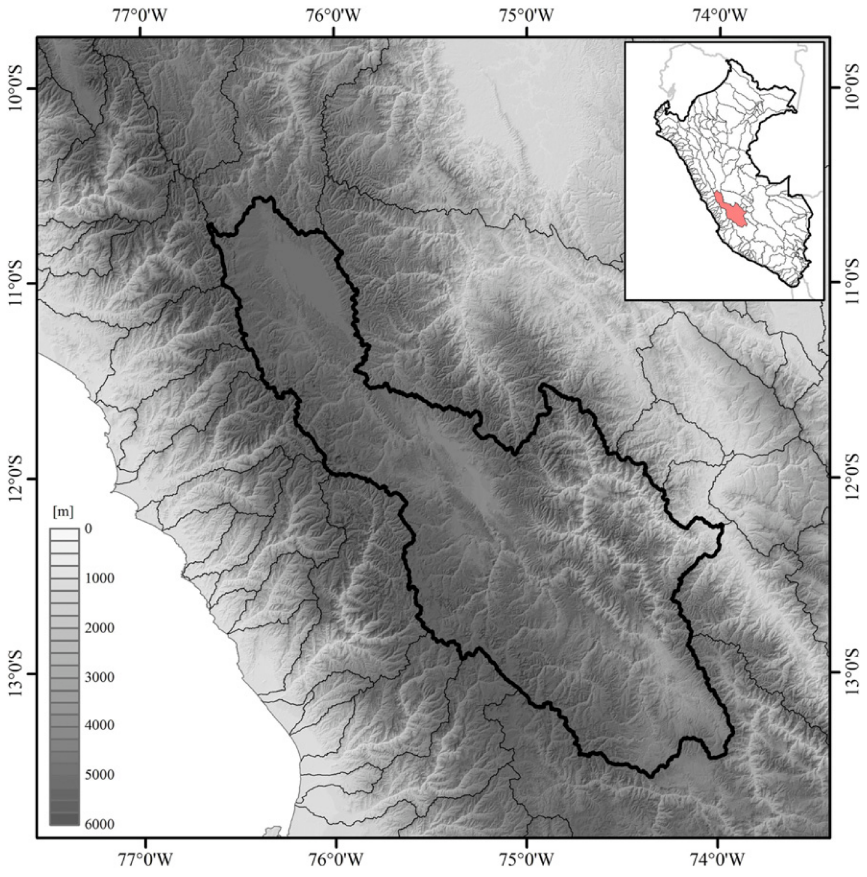

FIG. 1. Location of the Mantaro basin. The black line represents the boundary of MB. Gray shading represents the elevation (m MSL).

to several socioeconomic activities, such as agriculture, energy generation, and potable water supply.

Rainfall is the most difficult climatological variable to predict in the MB. One of the reasons for this difficulty is the considerable uncertainty introduced by the poor spatial resolution and short observational record of most datasets. For future scenarios, global climate models may hold some promise to give exciting perspectives for future rainfall projections; however, their coarse spatial resolution is inadequate for most local- to regional-scale applications, such as driving hydrological models. An alternative to solve this problem is development of empirical–statistical downscaling (ESD) techniques.

ESD techniques take advantage of existing relationships between large-scale fields (e.g., predictors) and local-scale surface variables (e.g., predictands) for the development of models that will be used for estimating the observed surface variables (Benestad et al. 2008). One advantage of ESD is that it can resolve finer spatial scales than dynamical methods and can be applied to parameters that cannot be directly obtained from regional climate models. The second advantage of ESD is its much higher computational efficiency than the dynamical downscaling, and thus it represents a low-cost method. However, one disadvantage of the ESD method is the requirement for long records of observational data to allow the model to be well trained and validated. Other problems of the ESD methods are that they tend to underestimate the magnitude of extreme events and that they assume that the currently observed relationship between local variables and large-scale fields remains constant under future scenarios, despite changing boundary conditions.

The seasonal prediction of DJF precipitation over the Peruvian Andes through empirical–statistical downscaling techniques has received relatively little attention (Yarleque et al. 2016; Wu et al. 2018). Wu et al. (2018) found that the Niño-3.4 index is not sufficient to predict precipitation over the southwestern Peruvian Andes, even though the Niño-3.4 index has a high correlation with precipitation in this region. Yarleque et al. (2016) developed a wavelet downscaling approach for the reconstruction of precipitation over the southeastern Peruvian Andes on decadal (10 calendar days) time scales, through the combination of data from in situ weather stations and normalized difference vegetation index data. However, none of these ESD models have considered as predictors Pacific Ocean SST, Atlantic Ocean SST, the Pacific convective regions [e.g., South Pacific convergence zone (SPCZ) and the intertropical convergence zone (ITCZ)], and the South Atlantic convergence zone (SACZ). All these large-scale climate features exert a

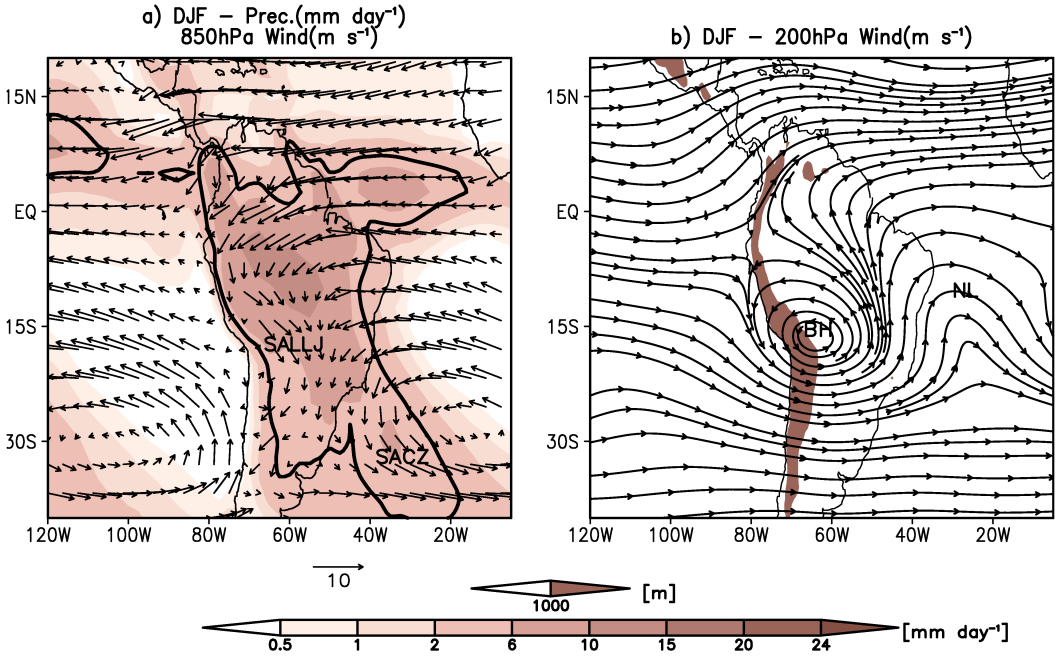

FIG. 2. Climatology of (a) 850-hPa wind ($m\,s^{-1}$) and precipitation ($mm\,day^{-1}$) and (b) 200-hPa wind ($m\,s^{-1}$; streamlines), during austral summer (DJF). The labeled features are defined in the text. GPCP precipitation and ERA-Interim reanalysis were used. Brown shading represents precipitation. The black contour in (a) represents the climatological isoline of 4 $mm\,day^{-1}$. Dark shading in (b) shows the location of the Andes. The analysis is based on 1980–2016.

strong influence on austral summer precipitation over South America (SA) and the Peruvian Andes region (see next section).

The main goal of this study is to develop an ESD model capable of predicting the spatial rainfall distribution in the central Peruvian Andes during austral summer. The main expectation of our research is that the results will contribute to the development of mitigation measures for extreme hydroclimatic events, including El Niño. For example, accurately predicting DJF precipitation anomalies over the central Peruvian Andes will help to mitigate any future negative impacts on local agriculture. Our current research is directed toward the development of statistical linkages between large-scale climate and regional rainfall that can be applied with output from seasonal climate forecast models.

In the following section, we discuss how our work builds on previous studies. Section 3 describes the data used. In section 4, we develop the design of the ESD model. Section 5 presents the results of the relationship between the estimated DJF precipitation anomalies and the chosen predictors for the 1982–2016 period as well as extreme El Niño episodes. The last section offers some concluding remarks.

2. Background

The South American monsoon system (SAMS) is one of the major monsoon systems in the Southern Hemisphere (Zhou and Lau 1998). It shows a distinct seasonal cycle with an onset during October, a mature phase between December and February, and demise in April (e.g., Marengo et al. 2001; Raia and Cavalcanti 2008; Garreaud et al. 2009; Marengo et al. 2012). During austral summer (DJF), the maximum precipitation falls over the south-central Amazon (Fig. 2a). In the upper troposphere (200 hPa), the Bolivian high and Nordeste low (BH–NL) system is the main feature over South America (Chen et al. 1999) (Fig. 2b). Silva Dias et al. (1983) show that latent heat, released during convection over the Amazon basin, determines the fundamental structure of the BH–NL system. Moreover, Lenters and Cook (1997) show that rainfall in the central Andes aids in further strengthening and displacing the BH southward. The BH–NL system disappears during the austral winter, once the upper-level westerly zonal flow is established over South America.

Precipitation over the South American continent is also characterized by a southeastward band of convective activity between the Amazon basin and the western South Atlantic (20°–40°S, 50°–20°W). This band is known as the SACZ. The SACZ is present all year; however, its maximum intensity occurs during the austral summer (Liebmann et al. 1999; Kodama 1992; Robertson and Mechoso 2000; Barreiro et al. 2002). The SACZ also modulates the intensity and forms the basic shape of the BH–NL system through the release of condensational heat to the upper troposphere. However, no studies exist documenting the direct influence of the SACZ on DJF precipitation in the MB. The propagation of midlatitude Rossby wave trains also modulates the SACZ on interannual time scales (Ma et al. 2011).

Another climatological feature related to the mature phase of the SAMS is the South American low-level jet (SALLJ;

TABLE 1. Indices of Pacific and Atlantic SST and tropical convective regions (SPCZ and ITCZ) used in this study.

No.	Label	Variable	Atmospheric teleconnection	
			Reduces precipitation over...	Favors precipitation over...
1	E	Index of eastern Pacific SSTA (Takahashi et al. 2011; http://www.met.igp.gob.pe/datos/EC.txt)	Eastern equatorial Amazon, Peruvian Altiplano and northwestern Bolivia (Sulca et al. 2018)	Coasts of central and northern Peru; entire coast of Ecuador; northeastern Peruvian Amazon; SESA (southernmost Brazil, northern Uruguay, eastern Paraguay, and northeastern Argentina) (Sulca et al. 2018)
2	C	Index of central Pacific SSTA (Takahashi et al. 2011; http://www.met.igp.gob.pe/datos/EC.txt)	Central and eastern equatorial Amazon; tropical Andes (Colombia, Ecuador, Peru, Bolivia, and northern Chile) (Sulca et al. 2018)	SESA, but more restricted over Uruguay and northeastern Argentina than in E (Sulca et al. 2018)
3	latE	Index of latitudinal SPCZ displacement (Vincent et al. 2011)	Northwestern and easternmost equatorial Amazon basin; southern Venezuela; southwestern Brazil; Western Cordillera of southern and central Andes of Peru (Sulca et al. 2018)	Northern coast of Peru; southern coast of Ecuador; central Brazil; Uruguay, Argentina, and central and northern Chile; northeastern Peruvian Amazon (Sulca et al. 2018)
4	latW	Index of longitudinal SPCZ displacement (Vincent et al. 2011)	Northern South America north of 3°S; Ecuador, southern Peru, Bolivian Altiplano, northern Chile, and northern Paraguay; central and northern coast of Peru, Western Cordillera of southern Peru, and Bolivian Altiplano (Sulca et al. 2018)	Eastern part of central Brazil; eastern slope of the central Andes of Peru (Sulca et al. 2018)
5	ITCZC	Index of latitudinal ITCZ displacement over central Pacific (Sulca et al. 2018)	Westernmost part of central equatorial Amazon basin and easternmost equatorial Amazon basin. The northern and central coast of Peru and the Ecuadorian Amazon basin (Sulca et al. 2018)	Northern Chile, Paraguay, southwestern Brazil, and along the northern coast of Brazil (Sulca et al. 2018)
6	ITCZE	Index of latitudinal ITCZ displacement over eastern Pacific (Sulca et al. 2018)	Northern Chile, northwestern Argentina, and northern coast of Brazil (Sulca et al. 2018)	Northern coast of Peru and southern coast of Ecuador, northern Andes of Peru, northern Chilean Andes, northeastern Argentina, Uruguay, and southernmost Brazil; southern Andes of Ecuador; northern Peruvian Amazon (Sulca et al. 2018)
7	ATL	Index of tropical Atlantic SSTA (80°W–10°E, 40°S–30°N; Vuille et al. 2000)	Amazon River basin (Enfield 1996; Misra 2004)	Northeastern Amazon basin; northern coast of Northeast Brazil, and Uruguay (Enfield 1996; Misra 2004)
8	SACZ	Index of convection over southern South America (65°–30°W, 40°S–0°; Barros et al. 2000)	Equatorial Amazon basin and equatorial Atlantic (Barreiro et al. 2002)	SESA and southernmost part of Northeast Brazil (Barreiro et al. 2002)

Montini et al. 2019). The SALLJ is located along the eastern slope of the Andes mountains between the surface and 700 hPa. The primary role of the SALLJ is the transport of warm and humid air from the Amazon basin toward southeastern South America (SESA). In addition, several studies found that the tropical convective regions (ITCZ and SPCZ) and Pacific SST can modulate the austral summer precipitation in the tropical Andes through equatorial and complex coupled waves (Chen et al. 1999; Sulca et al. 2018).

Here, we develop an ESD model that considers all of the abovementioned large-scale forcings as potential predictors for austral summer precipitation. The indices that we use to characterize these forcings are discussed below and are summarized in Table 1.

3. Data

To apply the ESD model on DJF rainfall over South America, we used daily gridded precipitation data from the CPC Global Unified Gauge-Based Analysis of Daily Precipitation (CPC_UNI; Chen et al. 2008). The CPC_UNI dataset presents a horizontal resolution of 0.5° × 0.5° and covers the 1979–2016 period. For Peru, we used the monthly gridded precipitation dataset called the Peruvian Interpolated Data of SENAMHI's Climatological and Hydrological

Observations (PISCO-SENAMHI), version 1.0 (Lavado et al. 2016). PISCO, version 1.0, has a horizontal resolution of 0.05° × 0.05° and covers the 1981–2016 period. PISCO data are based on the rain gauge network of the SENAMHI. We also considered the last version of the PISCO dataset (version 2.1; Aybar et al. 2019), which is based on different interpolation technique and coarser horizontal resolution (10 km × 10 km). To compare PISCO datasets, we performed a bilinear interpolation to the version 1.0 from 5 km × 5 km to 10 km × 10 km of horizontal resolution.

To analyze the relationship between the DJF large-scale atmospheric circulation and DJF precipitation anomalies over South America, we used ERA-Interim reanalysis from the European Centre for Medium-Range Weather Forecasts (ECMWF) (Dee et al. 2011). The ERA-Interim reanalysis presents a resolution of 0.75° × 0.75° and covers the 1979–2016 period. We focused on horizontal wind and geopotential height at 200 hPa. To quantify the linear relationship between precipitation and zonal wind anomalies over the MB at 200 hPa for the 1982–2016 period, we defined a 200-hPa zonal wind index (U200) as the average of mean DJF 200-hPa zonal wind inside the following box: 73.5°–76.75°W, 9.75°–14.25°S.

Below we briefly summarize the different indices used as large-scale forcing predictors of austral summer precipitation in our ESD model. More detailed information on these predictors can be found in Table 1.

To quantify the influence of DJF SST over the equatorial Atlantic Ocean on SA precipitation, we used monthly HadISST data (Rayner et al. 2003) at 1° × 1° for the period 1979–2016. We use the first rotated principal component (PC) of Atlantic SST anomalies in the region bounded by 80°W–10°E, 40°S–30°N (Vuille et al. 2000) as an index for Atlantic forcing (hereinafter referred to as ATL). The equatorial Atlantic SST has a positive linear relationship with precipitation over the equatorial Atlantic Ocean (Jauregui and Takahashi 2018).

To compute the convection index associated with the SACZ during austral summer, we used monthly gridded outgoing longwave radiation (OLR) data from NOAA/NCEP (Liebmann and Smith 1996). The OLR data present a spatial resolution of 2.5° × 2.5° for the period 1979–2016. We use the first PC of DJF OLR anomalies over eastern Brazil inside the region 65°–30°W, 40°S–0° (Barros et al. 2000) as an index for SACZ forcing (hereinafter referred to as SACZ).

We use two ENSO-related indices (E and C) to characterize the influence of El Niño. Takahashi et al. (2011) first defined these two orthogonal indices, which represent the variability of tropical sea surface temperature in the central and eastern equatorial Pacific (C and E, respectively). Large-scale climate anomalies associated with C and E episodes have been documented through atmospheric teleconnections, with significant impacts on precipitation in the Pacific Ocean and South America during austral summer (Sulca et al. 2018). Both C and E indices are available from the Instituto Geofísico del Perú (IGP) (http://www.met.igp.gob.pe/datos/EC.txt).

Variability related to convective activity over the SPCZ and ITCZ domains was analyzed by using four indices, referred to as the latW and latE indices over the SPCZ region and ITCZc and ITCZe indices over the Pacific ITCZ domain. LatW describes the longitudinal east–west displacement of the SPCZ, and latE is an index characterizing its latitudinal (north–south) displacement. The latitudinal (north–south) movement of the central portion of the Pacific ITCZ is measured by the ITCZc index, and the same displacement of the ITCZ over the eastern Pacific is tracked by the index ITCZe. All four indices were first defined in Sulca et al. (2018) and are known to significantly affect austral summer precipitation over Peru. All analyses are based on seasonal anomalies, with the climatological DJF (1982–2011) values being subtracted from the diagnostic fields of each individual DJF value (Wilks 2011).

4. ESD model architecture

Our empirical–statistical downscaling model is defined as the linear combination of the tropical Pacific Ocean SST, tropical Pacific convection, Atlantic SST, and SACZ forcings. We used the function *fitlm* in MATLAB that computes the linear-multiple-regression model (DuMouchel and O'Brien 1989) based on iterative reweighted least squares (Beaton and Tukey 1974).

The equation of the ESD model is

$$y_{(i,j,t)} = \sum_{n=1}^{8} \alpha_{(i,j,n)} X_{(n,t)} + \varepsilon_{(i,j,t)} \cdots, \tag{1}$$

where $X_{(t)}$ = {E, C, latE, latW, ITCZc, ITCZe, ATL, SACZ}, $y_{(i,j,t)}$ represents the target variable (the predictand) that varies with time t; $X_{(n,t)}$ represents the time series of eight predictors, and $\alpha_{(i,j,n)}$ represent the least squares regression parameters (intercept of the ESD model and slope of each predictor, respectively). The local regression parameters (α_1 and α_2) are estimated by minimizing the model error $\varepsilon_{(i,j,t)}$. The subscripts i and j represent longitude and latitude, respectively. Here, the calibration period is 1982–2006 and the validation period is 2007–16.

The statistical significance of the ESD model was assessed using the version of the Student's t test for iterative reweighted least squares regression (Beaton and Tukey 1974). However, since the sample size is small (35 summers) and the few extreme El Niño events (Takahashi et al. 2011) can lead to an overestimation of the significance in some areas of SA, the information from the significance test was used mainly to guide our focus on specific regions of interest.

We also examined the physical mechanisms to establish whether the observed statistical relationship is dynamically plausible. The statistical significance at the 90% confidence level of the regression coefficients is provided by the *regress* function in MATLAB (Chatterjee and Hadi 1986). To quantify the performance of the ESD model, we computed the root-mean-square error (RMSE) for each grid point for the 2007–16 period.

Florax and Folmer (1992) pointed out that spatial distribution of precipitation is a source of uncertainty in statistical precipitation models at the local scale. Sangati and Borga (2009) highlighted this problem as the main source of uncertainty in local-scale hydrological modeling. Hence, the ESD

TABLE 2. List of experiments applied in this study.

Expt	Predictors included	Design motivation
Exp-1	E and C	Are ENSO predictors (E and C) sufficient to estimate the DJF precipitation patterns over South America?
Exp-2	latE, latW, ITCZc, and ITCZe	Do indices of Pacific convective regions (SPCZ and ITCZ) outperform ENSO indices as predictors for DJF precipitation over South America?
Exp-3	ATL and SACZ	How do Atlantic SST and SACZ forcings compare with Pacific convective region and ENSO indices in estimating DJF precipitation over South America?
Exp-4	C, E, latE, latW, ITCZc, ITCZe, and ATL	What is the contribution of SACZ forcing to DJF precipitation over South America?
Exp-5	C, E, latE, latW, ITCZc, ITCZe, and SACZ	What is the contribution of tropical Atlantic SST to DJF precipitation over South America?
Exp-6	ITCZc, ITCZe, ATL, and SACZ	How well do the joint ITCZ, SACZ, and Atlantic SST forcing predict DJF precipitation over South America?
Exp-7	E, C, and ATL	Are SST indices from the tropical Pacific and Atlantic sufficient to reproduce DJF precipitation over South America?
Exp-8 (ESD)	E, C, latW, latE, ITCZe, ITCZc, ATL, and SACZ	To what extent can the combination of all forcings predict DJF precipitation over South America?

model also varies in space, which we investigate further using the Mantaro basin as a case study.

Several previous studies also found spatial variations using several types of linear-regression models (Florax and Folmer 1992; Diack 1999; Jiang et al. 2019; Sharifi et al. 2019). For instance, Florax and Folmer (1992) defined a weight function to compute linear-spatial-regression models [Eq. (2)]. They consider the following general solution for the linear-regression model for spatial cross sections r (=1, 2, . . . , R):

$$\mathbf{y}_2 = \zeta \mathbf{W}\mathbf{y} + \mathbf{X}\boldsymbol{\beta} + \mathbf{W}\mathbf{X}^*\boldsymbol{\rho} + \boldsymbol{\varepsilon}\cdots, \tag{2}$$

where $\boldsymbol{\varepsilon} = \lambda \mathbf{W}\boldsymbol{\varepsilon} + \boldsymbol{\mu}$, $\mathbf{y}_2$ is the target variable ($R \times 1$), $\mathbf{W}$ represents the spatial weights matrix ($R \times R$), $\mathbf{X}$ is the matrix of nonstochastic regressor ($R \times k$), $\mathbf{X}^*$ represents the matrix of explanatory variables with the constant term deleted [$R \times (k-1)$], ζ represents the autocorrelation coefficient, $\boldsymbol{\beta}$ represents the vector of coefficients of the nonweighted independent variables ($k \times 1$), $\boldsymbol{\rho}$ represents the [$(k-1) \times 1$] vector of cross-correlation coefficients, λ is the

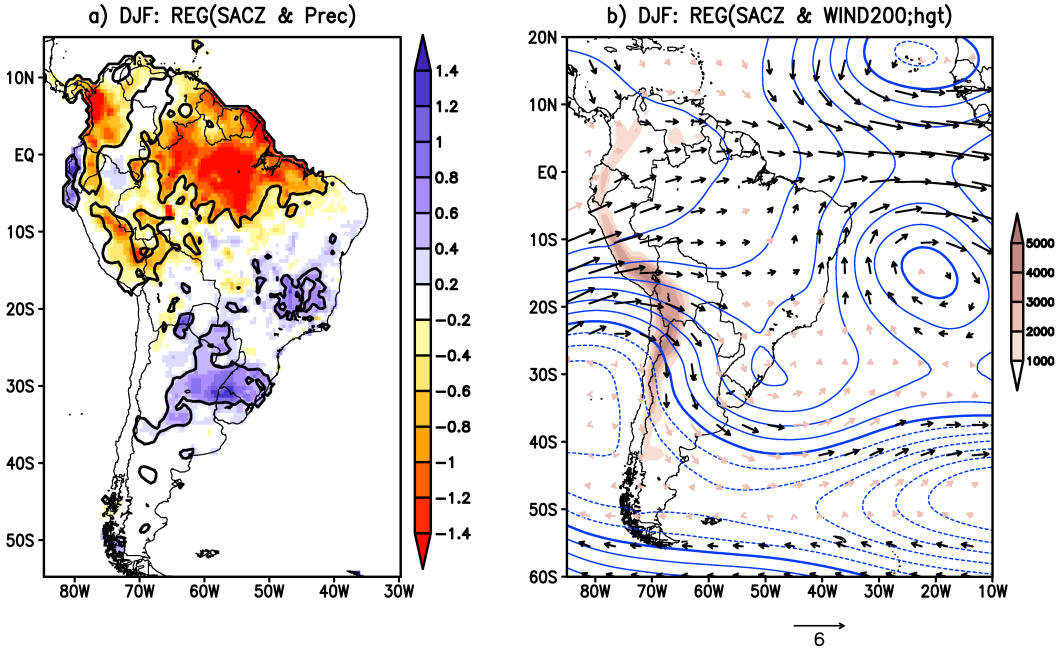

FIG. 3. Regression between standardized SACZ time series and (a) DJF precipitation (mm day^{-1}) anomalies and (b) anomalous wind (m s^{-1}) and geopotential height (m) over South America at 200 hPa. Black vectors are statistically significant at the 90% confidence level. Black contours represent significant regression between SACZ index and precipitation at the 90% confidence level. The contour interval of geopotential height anomalies is 30 m. Brown shading represent the topography of the Andes. The analysis is based on the 1982–2016 period. ERA-Interim and CPC_UNI datasets were used in this analysis.

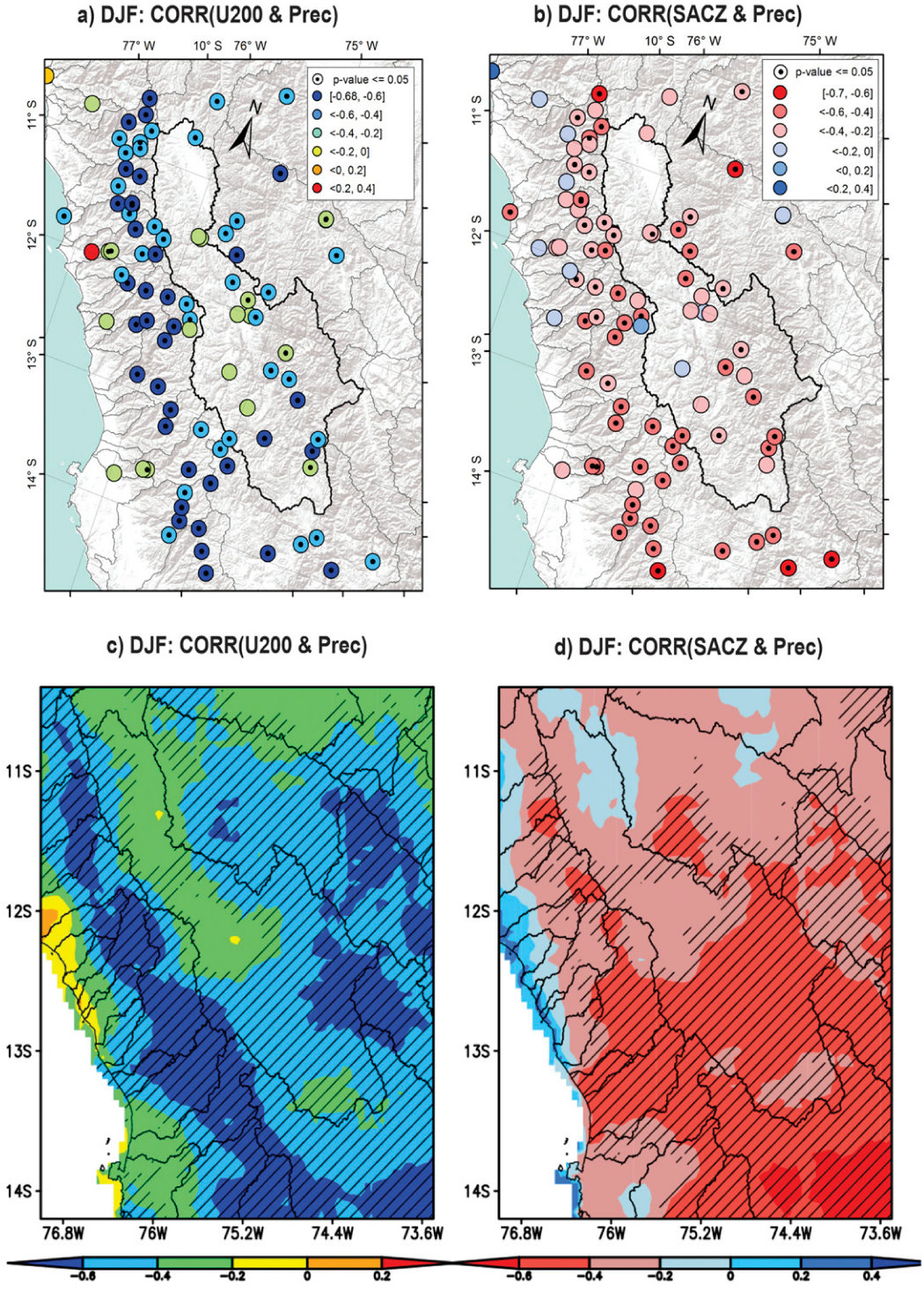

FIG. 4. Correlation between precipitation (mm day^{-1}) anomalies over the central Andes of Peru and (a),(c) the index of 200-hPa zonal wind (U200; m s^{-1}) and (b),(d) SACZ (W m^{-2}) during the austral summer (DJF) for the 1982–2016 period. Dotted circles and hatching represent statistically significant correlations at the 95% confidence level. Rain gauge stations used in the PISCO v1.0 dataset were used in this analysis.

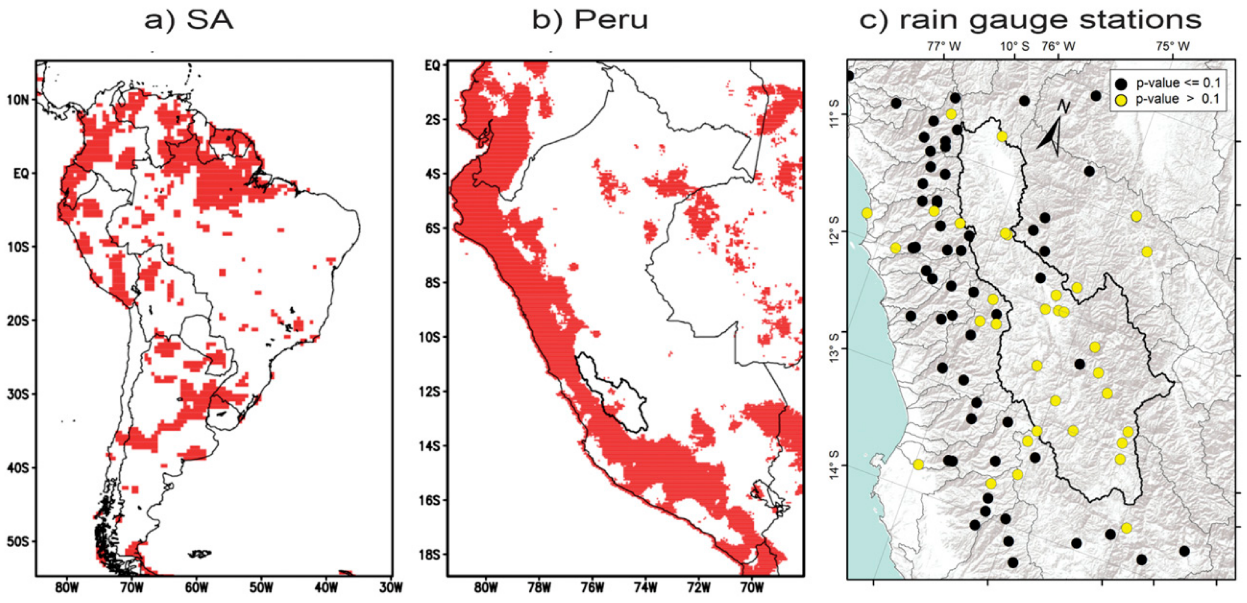

FIG. 5. Red areas represent regions within (a) South America and (b) Peru where the F test indicates that the ESD model is statistically significant at the 90% level for the 1982–2006 period. (c) Black circles represent rain gauge stations in and around the MB where an F test indicates statistical significance of the ESD model at the 90% level for the 1982–2006 period. Yellow circles indicate stations where the ESD model is not significant at the 90% level. The black line represents the boundary of the MB. CPC_UNI [in (a)] and PISCO v1.0 [in (b)] datasets were used in this analysis. Rainfall stations from the PISCO v1.0 dataset [in (c)] were used in this analysis.

coefficient of the autoregressive error term, and $\boldsymbol{\mu}$ is a vector of random errors with $E(\boldsymbol{\mu}) = 0$ and $E(\boldsymbol{\mu} \cdot \boldsymbol{\mu}') = \sigma_{\mu}^2 \mathbf{I}$.

Moreover, Florax and Folmer (1992) and Sharifi et al. (2019) pointed out that an aleatory criterion of the users can define the weight function **W**. For instance, Jiang et al. (2019) defined their weight function as a linear-regression model of local parameters, such as elevation, slope, and land use. Sharifi et al. (2019), on the other hand, used the function weight generated by the same artificial neural network. In this study, the weight function for the DJF precipitation anomalies over the central Peruvian Andes is the pattern of correlation between precipitation and zonal wind at 200 hPa.

To analyze the contribution of each forcing in the ESD model to estimate DJF precipitation and the regional atmospheric circulation anomalies over SA, we performed eight different experiments. These different model experiments allow us to isolate the contribution of specific forcings such as the role of the tropical Pacific or Atlantic Ocean. The different forcing combinations used in our experiments are listed in Table 2. Last, we used the El Niño 2015/16 as a case study to highlight the role of all forcings in contributing to the anomaly patterns of precipitation and upper-level regional atmospheric circulation over SA in the ESD model during this event.

5. Results and discussion

a. *Impacts of the SACZ on precipitation and upper-level regional atmospheric circulation over South America during austral summer*

Figure 3a shows the influence exerted by the SACZ on DJF precipitation through regression analysis. A significant reduction in precipitation is apparent over northern Venezuela, the central and eastern equatorial Amazon basin, and the tropical Andes (Colombia, Ecuador, Peru, and northern Bolivia) while a statistically significant increase can be observed over central and northern Argentina and SESA (Uruguay, Paraguay, and southernmost Brazil). The pattern of DJF precipitation anomalies is consistent with the predominance of upper-level westerly wind anomalies over entire SA north of 20°S, an upper-level Kelvin wave response over the equatorial Atlantic Ocean, and an upper-level anticyclonic anomaly over SESA (Fig. 3b). These results are consistent with previous modeling studies regarding the impact of the SACZ on DJF precipitation anomalies over SA, which also show a weakening of the BH–NL system and the development of an upper-level anomalous anticyclonic circulation over SESA during the austral summer (Chen et al. 1999; Barros et al. 2000; Barreiro et al. 2002).

b. *Relationship between SACZ and zonal wind at 200 hPa with precipitation over the Mantaro basin during the austral summer*

Figures 4a and 4c show the correlation between 200 hPa zonal wind (U200) anomalies and precipitation P (e.g., rainfall gauge stations and PISCO v1.0 datasets) over the Mantaro basin during austral summer for the 1982–2016 period. Figure 4a displays that P–U200 correlations are lower than -0.4 ($p < 0.1$) over the highland regions of the MB and the western Mantaro valley but the correlations are lower than -0.6 ($p < 0.1$) over the southern MB, eastern Mantaro valley, and the Western Cordillera of the central Andes of Peru. This P–U200 correlation pattern is mirrored by the PISCO v1.0 data (Fig. 4c). Figure 4c portrays that the P–U200 correlations present negative values lower than -0.6

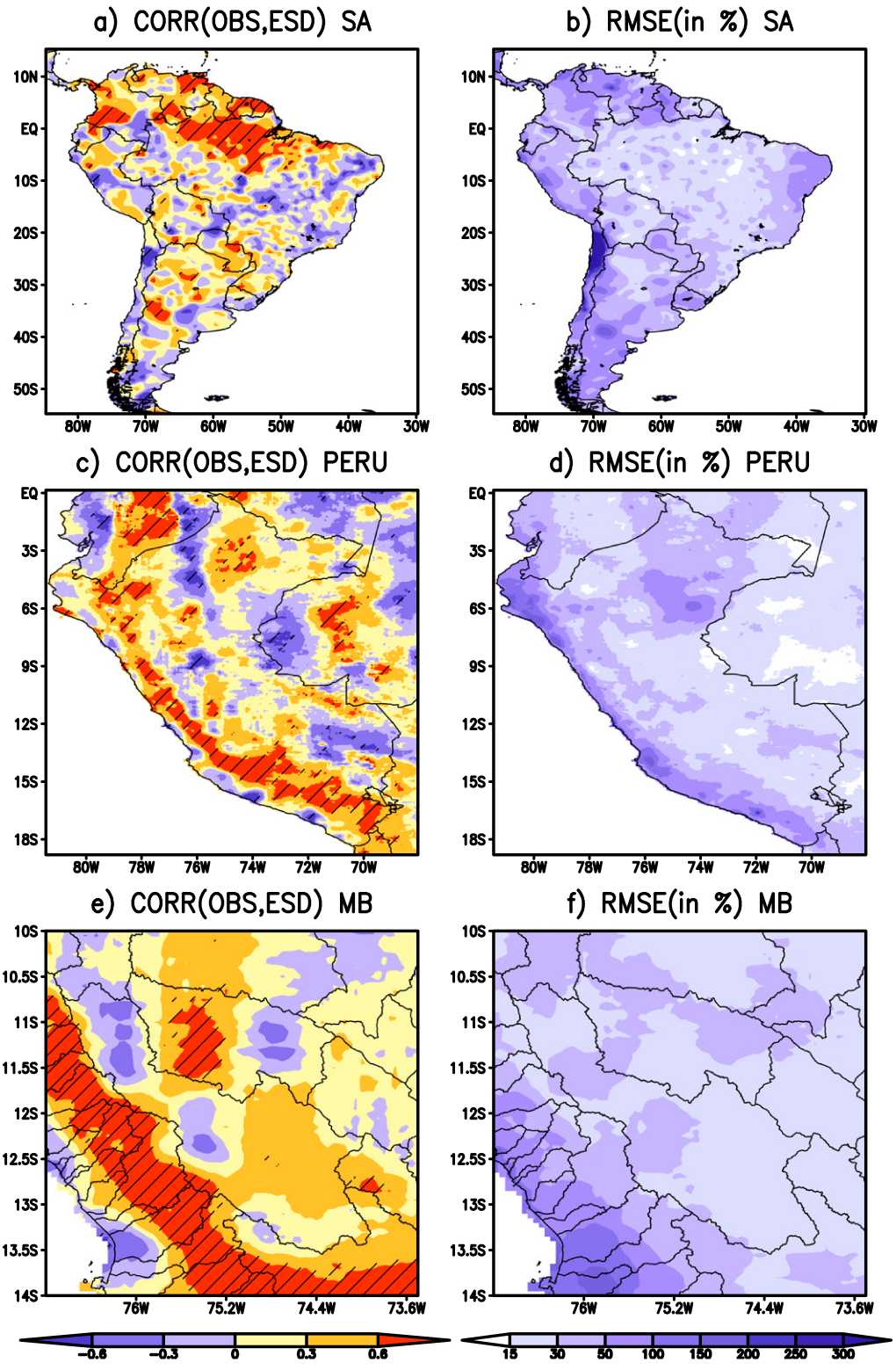

FIG. 6. Correlation between observed and estimated DJF precipitation anomalies over (a) South America, (c) Peru, and (e) MB, and the RMSE between observed and ESD-estimated DJF precipitation anomalies (%) over (b) South America, (d) Peru, and (f) MB. Hatching represents statistically significant correlations at the 90% confidence level. CPC_UNI [in (a) and (b)] and PISCO v1.0 [in (c)–(f)] datasets were used in this analysis. The analysis is based on the 2007–16 period.

TABLE 3. List of averaged squared correlation r^2 and averaged RMSE (%) inside the limits of the MB for all experiments performed in this study. The validation period is 2007–16.

Expt	Avg r^2	Avg RMSE (%)
Exp-1	0.16	22.58
Exp-2	0.14	29.65
Exp-3	0.31	21.28
Exp-4	0.16	33.18
Exp-5	0.18	33.89
Exp-6	0.18	28.01
Exp-7	0.16	23.97
ESD (Exp-8)	0.18	34.4

over the entire MB and along the Western Cordillera of the central Peruvian Andes. However, the western part of the central MB does not present statistically significant correlations where there are no rain gauge stations, while the correlations over the eastern part of the southern MB are statistically significant. These results support previous studies about the relationship between 200-hPa zonal wind and precipitation over the central Peruvian Andes (Sulca et al. 2016) and even in the Altiplano region farther south (e.g., Minvielle and Garreaud 2011). These same results are also consistent with the notion that this negative linear relationship between U200 and P still prevails to the north of the MB, such as over the Cordillera Blanca (Vuille et al. 2008). This negative linear relationship also has potential to contribute to the development of ESD models for precipitation over the central Peruvian Andes, as was done over the Altiplano region (e.g., Minvielle and Garreaud 2011).

The results of the correlation between SACZ and DJF precipitation anomalies in rain gauge stations and the PISCO v1.0 dataset within the Mantaro basin for the 1982–2016 period are shown in Figs. 4b and 4d, respectively. Figure 4b displays the predominance of negative correlations over the entire central Peruvian Andes (<-0.2) in rain gauge stations, but only along the Western Cordillera of the central Andes of Peru are they significant. The DJF SACZ-P correlation pattern is mirrored in the PISCO v1.0 dataset (Fig. 4d). However, the negative correlations are only statistically significant over the central part of the MB and along the Western Cordillera of the central Andes of Peru, consistent with the results from rain gauge stations located south of 14.2°S and along the Western Cordillera of the central Peruvian Andes. All these results suggest that the SACZ may be able to modulate the intensity of the mean DJF precipitation over the entire central Peruvian Andes. Still, the relationship is only significant south of the MB and over the Western Cordillera of the central Peruvian Andes.

c. *Validation of the ESD model*

The results of the significance test (F test) of the ESD model for the DJF precipitation anomalies over SA and Peru for the 1982–2006 period are shown in Fig. 5. Figure 5a shows that the

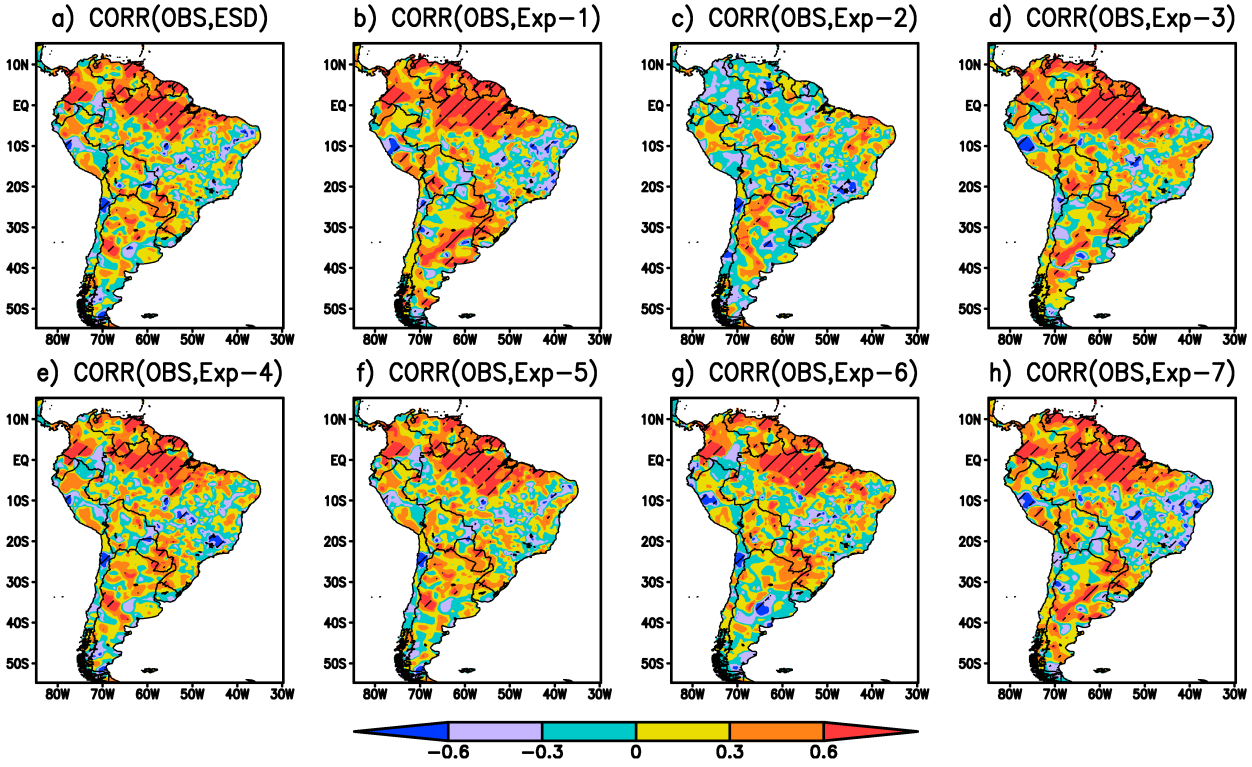

FIG. 7. Correlation between observed and estimated DJF precipitation anomalies for the (a) ESD, (b) Exp-1, (c) Exp-2, (d) Exp-3, (e) Exp-4, (f) Exp-5, (g) Exp-6, and (h) Exp-7 models. The analysis is based on the 2007–16 period. CPC_UNI precipitation was used in this analysis. Hatching indicates statistically significant correlations at the 90% confidence level.

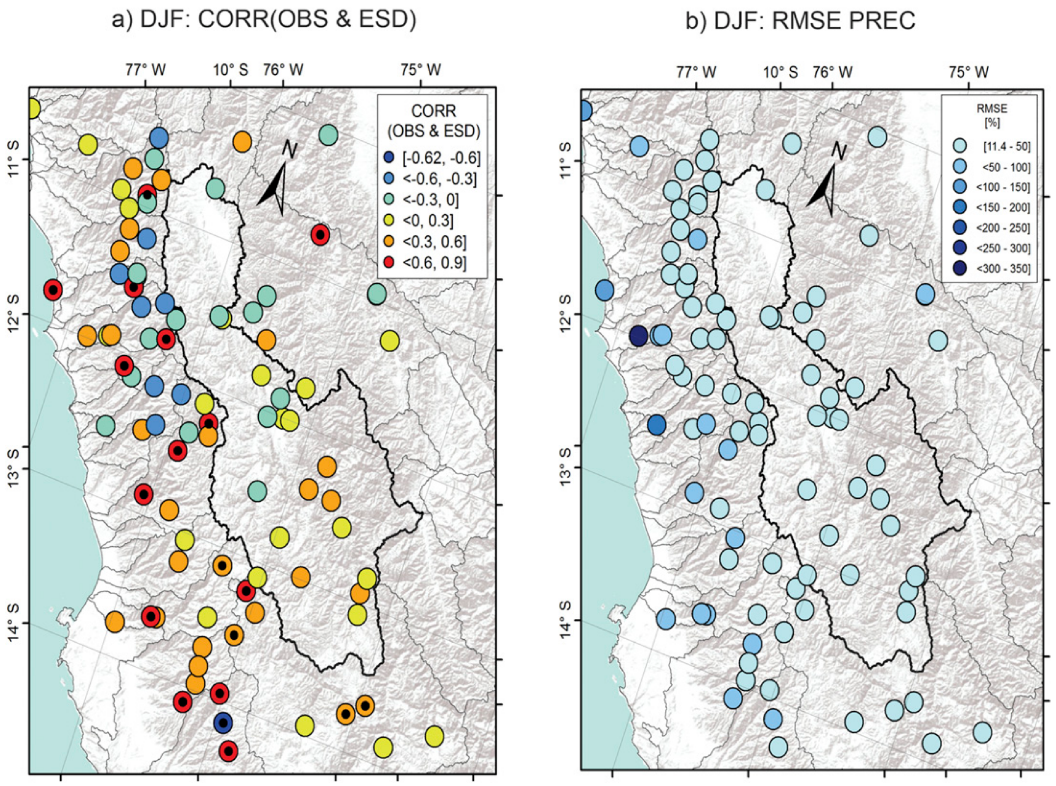

FIG. 8. (a) Correlation between observed and estimated DJF precipitation anomalies in and around the MB. (b) RMSE (%) between observed and ESD model-estimated DJF precipitation anomalies in and around the MB. Dotted circles represent statistically significant correlation at the 90% confidence level. Rain gauge stations from PISCO v1.0 dataset were used in this analysis. The analysis is based on the 2007–16 period.

ESD model is statistically significant in a few regions of SA, such as the central and eastern equatorial Amazon basin, the tropical Andes (Colombia, Ecuador, Peru, and northern Bolivia), the coast of northern Peru and Ecuador, and the central part of the western Argentinian Andes. Over Peru the ESD model has significant explanatory power along the Western Cordillera of the tropical Andes, the coast of northern Peru, the coasts and central Andes of Ecuador, and the Peruvian Amazon around 4.2°S, 73.6°W (Fig. 5b). Finally, Fig. 5b also shows that the ESD model only estimates the precipitation anomalies accurately over the southeastern MB and along the Western Cordillera of the central Peruvian Andes. The significance field of the full ESD model with the gridded PISCO data is consistent with the results obtained when repeating the analysis with rain gauge data (Fig. 5c). Hence, the ESD model cannot faithfully estimate DJF precipitation over the entire MB, likely due to the lack of rain gauge stations.

To validate the performance of our ESD model, we performed a correlation analysis between observed and estimated DJF precipitation anomalies over SA, Peru, and the MB for the 2007–16 period (Fig. 6). Figure 6a highlights the predominance of statistically significant positive correlations, higher than 0.6, over the central and eastern equatorial Amazon basin, parts of the Colombian and Ecuadorian Andes, and the central part of the eastern Argentinian Andes. Similar results are observed for all experiments, except Exp-2 (Table 3), which does not present significant correlations (Fig. 7).

Figure 6c shows that the entire tropical Andes (Ecuador, Peru, and northern Bolivia) and the central Peruvian Amazon present statistically significant positive correlations, which are higher than 0.5 ($p < 0.1$), in the PISCO v1.0 dataset. This correlation pattern resembles the results from the significance test for the ESD model over Peru, except along the northern coast of Peru, the coast of Ecuador, and the Peruvian Altiplano (Fig. 6a). Hence these results indicate that the ESD model predicts DJF precipitation adequately along the entire tropical Andes (Ecuador, Peru, and northern Bolivia).

At the local scale, Fig. 6e indicates statistically significant positive correlations along the Western Cordillera of the central Peruvian Andes. This correlation pattern is consistent with the correlation between observed and estimated DJF precipitation anomalies when using all rain gauge stations over the MB (Fig. 8a). Figure 8a indicates the presence of positive correlations (>0.6) over the southern and central parts of the Western Cordillera of the central Peruvian Andes, and even over the southwestern Peruvian Amazon basin. More interestingly, this correlation pattern is similar to the results obtained from the *F* test when applied to the ESD model and the SACZ-P correlation over the MB. Hence, all these results suggest that the ESD model cannot improve the prediction of

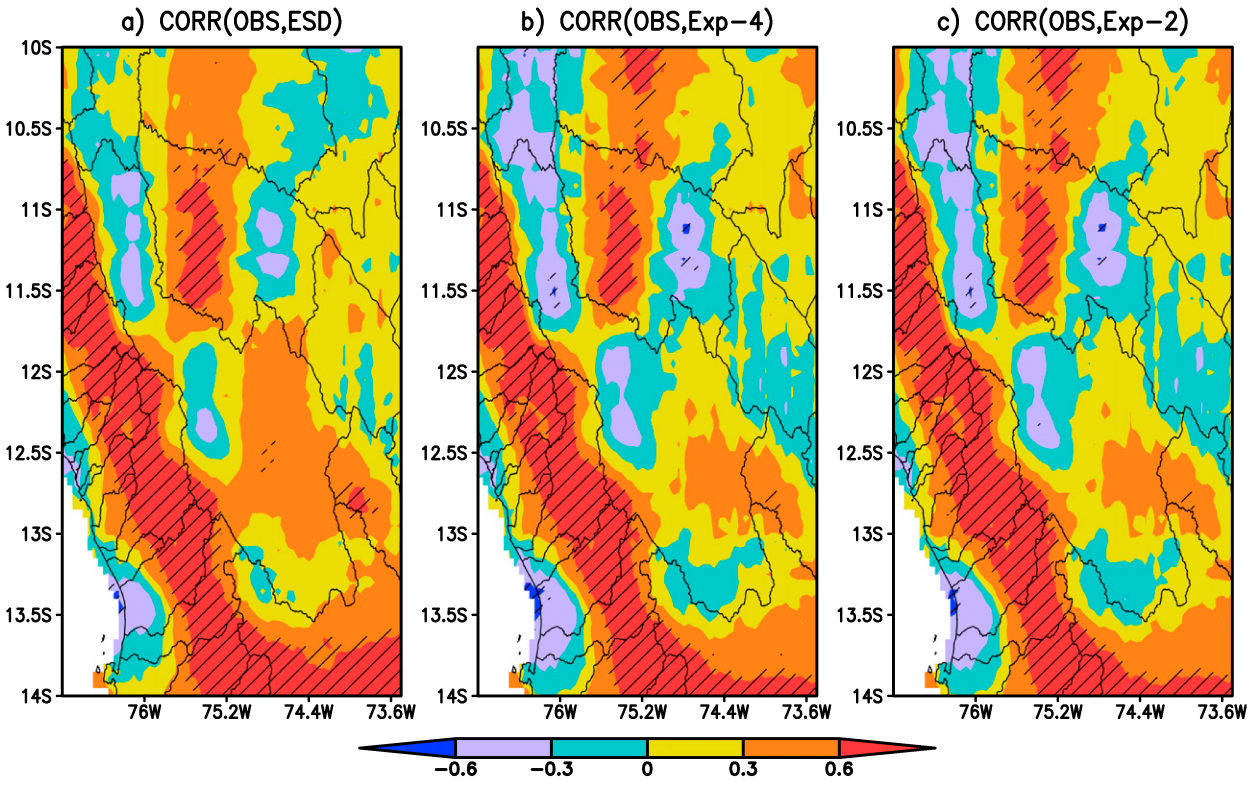

FIG. 9. Correlation between observed and estimated DJF precipitation anomalies for (a) ESD, (b) Exp-4, and (c) Exp-2. The analysis is based on the 2007–16 period. The PISCO v1.0 dataset was used in this analysis. Hatching indicates statistically significant correlations at the 90% confidence level.

DJF precipitation over the MB due to a lack of rain gauge stations that cover its entire area. Conversely, the ESD model can predict the DJF precipitation along the Western Cordillera of the central Peruvian Andes. Although this correlation pattern is also observed for the Exp-2 and Exp-4 models, both these experiments present correlations that are lower than 0.6 over the southern and central parts of the MB, and they are not capable of correctly estimating the sign of the DJF precipitation anomalies (Fig. 9). Since Exp-2 and Exp-4 present slightly lower correlations over entire MB than in the ESD model, we chose to focus only on the ESD model in the remaining analyses.

d. Limitations of the ESD model

The results in section 5c highlighted several limitations of the ESD model. For one, the lack of long observational time series and the sparse observational network over several regions of complex topography, such as tropical Andes, limit the ability to properly train the ESD model over a dense network of stations consisting of long records.

Second, Fig. 5a shows weak and even negative correlations over the rest of SA, such as the western and central parts of the Amazon basin and eastern Brazil, suggesting that other factors besides the ones included in our model, influence DJF precipitation. Indeed, Misra et al. (2002), who used regional climate simulations to understand the moisture budget over entire SA, pointed out that moisture flux convergence determines most of the interannual variability of DJF precipitation over the Amazon basin, the Atlantic intertropical convergence zone, and northeastern Brazil. Moreover, Misra et al. (2002) found that surface evaporation and surface flux convergence play a critical role in determining interannual variability of DJF precipitation over the southern Pampas, the Gran Chaco area, and the SACZ. However, we do not analyze these aspects here as they are beyond the scope of the present study.

Third, deficiencies of the ESD model in estimating DJF precipitation along the coast of northern Peru and Ecuador, over the eastern slope of the Peruvian Andes, and southern Peru are apparent (Fig. 5b). The deficiency along the coast of northern Peru and Ecuador is likely due to the lack of local forcings in the model that can play a critical role during coastal El Niño episodes (Echevin et al. 2018; Takahashi and Martínez 2019; Hu et al. 2019; Rodríguez-Morata et al. 2019). The lack of significance to the east of the Peruvian Andes, such as the Peruvian Amazon, may reflect the lack of rain gauge stations (e.g., Lavado et al. 2016). Fourth, Fig. 5c suggests that lack of rain gauge stations in the current version of the PISCO dataset presents a limitation for the development of spatially distributed multiple-regression models to estimate the DJF precipitation over the Mantaro basin.

e. RMSE analysis of the ESD model

The results of the RMSE analysis of the ESD model are shown in Figs. 6b, 6d, and 6f. Figure 6b displays the predominance of a RMSE higher than 50% over entire SA, but the

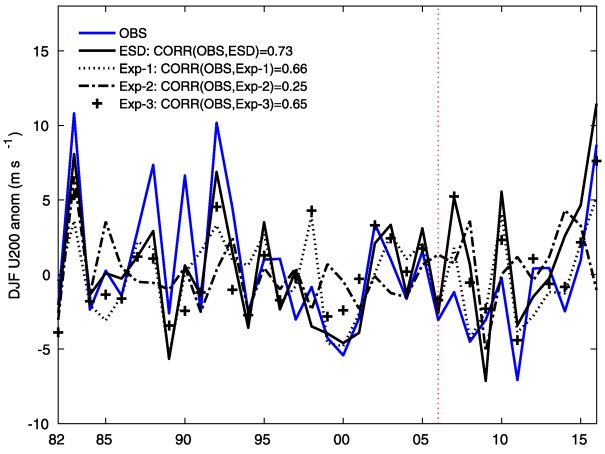

FIG. 10. Time series of the 200-hPa DJF zonal wind anomaly index ($m\,s^{-1}$; 1982–2016) for observations (blue line) and estimated by the ESD model (black solid line), Exp-1 (black dotted line), Exp-2 (black dash–dotted line), and Exp-3 (black plus sign).

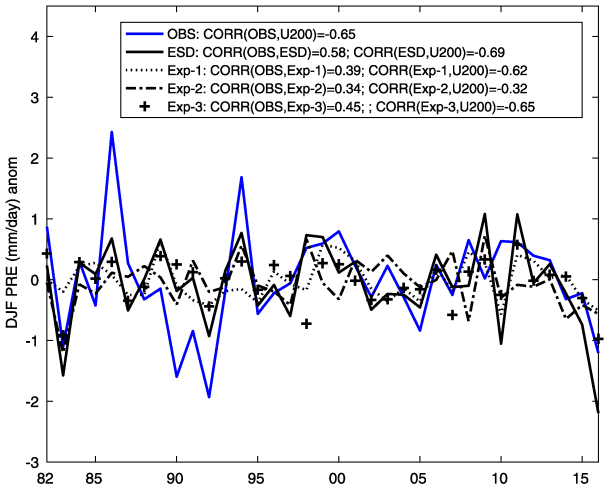

FIG. 11. Time series of the DJF precipitation anomaly index ($mm\,day^{-1}$; 1982–2016) for observations (blue line) and estimated by the ESD model (black solid line), Exp-1 (black dotted line), Exp-2 (black dash–dotted line), and Exp-3 (black plus sign). OBS represents the observed DJF precipitation anomaly index. U200 represents the observed DJF zonal wind anomaly index. The term CORR indicates Pearson correlation.

maximum RMSE is observed over the northern Chilean Andes, southern Argentina, and northern Venezuela (>100%). All these results show that the ESD model overestimates the intensity of the observed DJF precipitation over entire SA. For Peru, Fig. 6d shows that the coast of northern Peru, the Western Cordillera of the Peruvian Andes, and the Peruvian Amazon present a positive RMSE of less than 10%. Over the MB, the RMSE is below 10% on its western side, the central part of the northern MB, the western side of the MB, and along the Western Cordillera of the central Andes of Peru (Fig. 6f). This latter pattern is mirrored in the RMSE of the rain gauge stations in and around the MB, with positive RMSE values lower than 50% over the entire MB (Fig. 8b). In comparison, the RMSE in Western Cordillera of the central Peruvian Andes is around 50%, except for its western side, where the values are between 50% and 100%.

An additional statistical analysis contrasts the squared correlation r^2 and RMSE averaged within the limits of the Mantaro basin. Table 3 displays that the ESD model presents an averaged r^2 of 0.18, while the rest of the experiments show averaged r^2 values that vary between 0.14 and 0.31. The averaged RMSE of the ESD model is 34.4%, while the rest of the experiments present an averaged RMSE lower than 30% (Table 3). Even though the ESD model shows only an intermediate averaged r^2, and the highest averaged RMSE, the ESD model performs well when estimating precipitation anomalies over the entire central Peruvian Andes, in contrast to Exp1–7 (figures not shown).

f. Estimation of DJF 200 hPa zonal wind and precipitation anomalies over the MB

Figure 10 shows the interannual variability of the observed and estimated (ESD model, Exp-1, Exp-2, and Exp-3) time series of the spatially averaged mean DJF U200 index inside the following box: 73.5°–76.75°W, 9.75°–14.25°S. The ESD model simulates the interannual variability of observed DJF U200 reasonably well ($r = 0.72$; $p < 0.05$), while the other experiments result in correlations of $r < 0.66$. The latter is a further indication that the ENSO signal is an essential modulator of the upper-level zonal wind over South America (Chen et al. 1999).

Figure 10 further indicates that the maximum observed DJF U200 westerly wind anomalies ($>+5\,m\,s^{-1}$) occur in 1982/83, 1987/88, 1989/90, 1991/92, and 2015/16. Conversely, the maximum easterly wind anomalies ($<-3\,m\,s^{-1}$) were registered in 1999/2000, 2000/01, 2007/08, and 2010/11. The years 2000/01 and 2007/08 coincided with strong La Niña episodes. Figure 10 also displays that the ESD model, Exp-1, Exp-2, and Exp-3 all underestimate the observed intensity of DJF U200, as can be expected from linear-regression models.

The interannual variability of the observed and estimated (ESD model, Exp-1, Exp-2, and Exp-3) time series of mean DJF precipitation (spatially averaged inside the box covering 77.5°–73.5°W, 9.75°–14.25°S) is shown in Fig. 11. The ESD model simulates the interannual variability of observed DJF precipitation reasonably well ($r = 0.58$; $p < 0.05$), while the other experiments result in correlations of $r < 0.45$. Figure 11 also shows that the precipitation estimated by the ESD model has the highest negative correlation with observed DJF U200 ($r = -0.69$; $p < 0.05$), while the other experiments present correlations lower than −0.65. These results indicate that the ESD model represents the best option out of the eight experiments for estimating DJF precipitation over the central Peruvian Andes.

g. Estimating precipitation and large-scale atmospheric circulation anomalies over South America during austral summers associated with extreme El Niño episodes

The observed and estimated DJF precipitation anomalies over South America and the Mantaro basin during the three

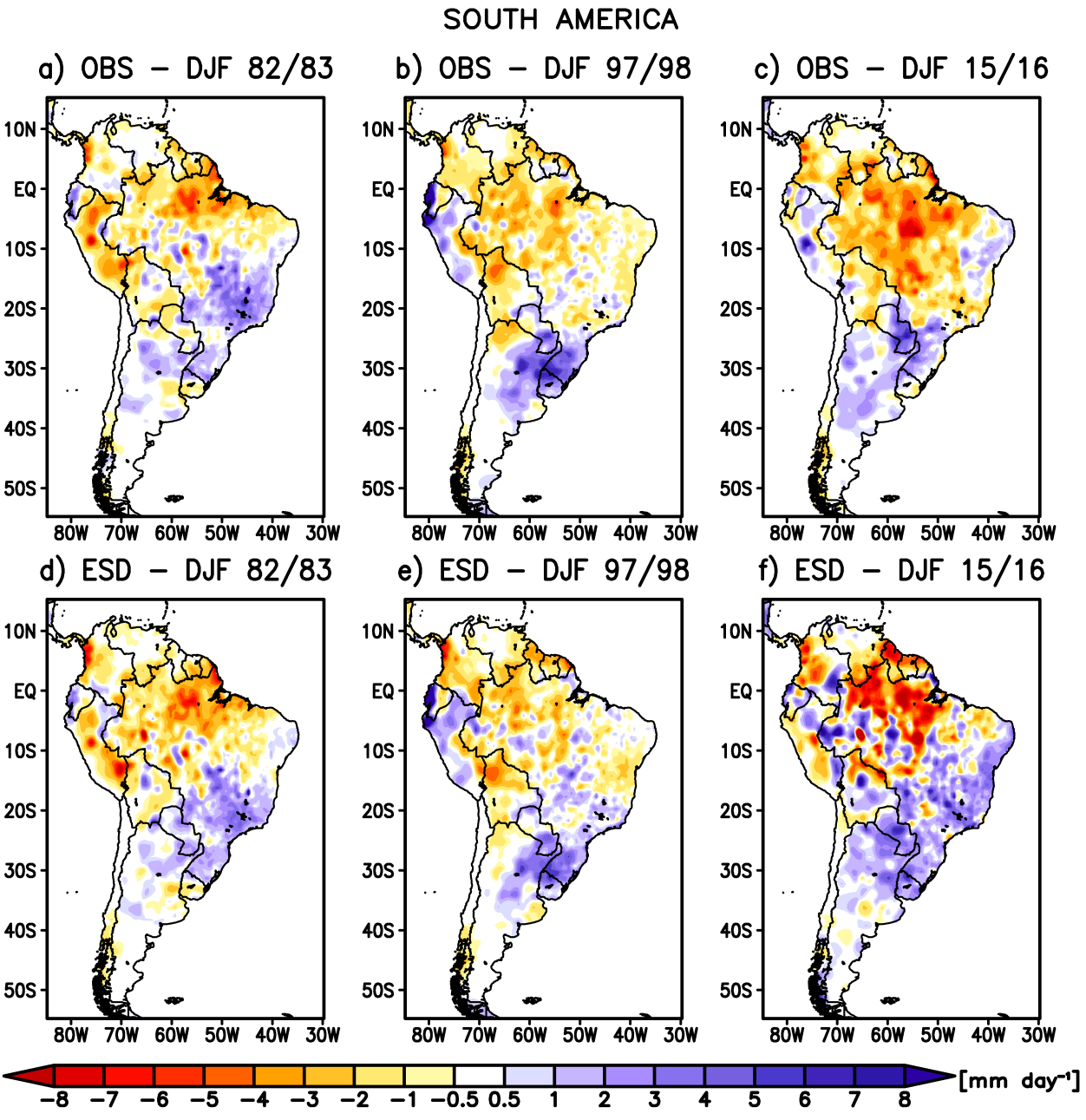

FIG. 12. DJF precipitation anomalies (mm day^{-1}) over South America for the three extreme El Niño episodes: (left) 1982/83, (center) 1997/98, and (right) 2015/16 (a)–(c) in the observed dataset and (d)–(f) estimated by the ESD model. The CPC_UNI dataset was used in this analysis.

extreme El Niño episodes 1982/83, 1997/98, and 2015/16 are shown in Figs. 12 and 13, respectively. Figure 12a shows that DJF 1982/83 was characterized by wet anomalies along the coasts of northern Peru and southern Ecuador, central-eastern Brazil, and SESA (e.g., central and northern Argentina, Paraguay, and Uruguay), while dry anomalies were observed over the entire equatorial Amazon. This precipitation pattern is well reproduced by the ESD model, even though it slightly overestimates rainfall over Paraguay and the northernmost part of Northeast Brazil (Fig. 12d). Figure 13a shows that the entire Mantaro basin was dry, except along its northeastern boundary. The ESD model reproduces this pattern very well, although DJF precipitation is slightly (less than -0.5 mm day^{-1}) overestimated (Fig. 13d).

In DJF 1997/98 wet anomalies occurred along the coasts of northern Peru, Ecuador, and SESA (e.g., northernmost Argentina and Uruguay), while dry anomalies prevailed over the entire equatorial and western Amazon basin (Fig. 12b). As shown in Fig. 12e, this precipitation pattern is quite accurately reproduced by the ESD model, even though it computes wet anomalies over the southeastern Amazon basin and overestimates the intensity

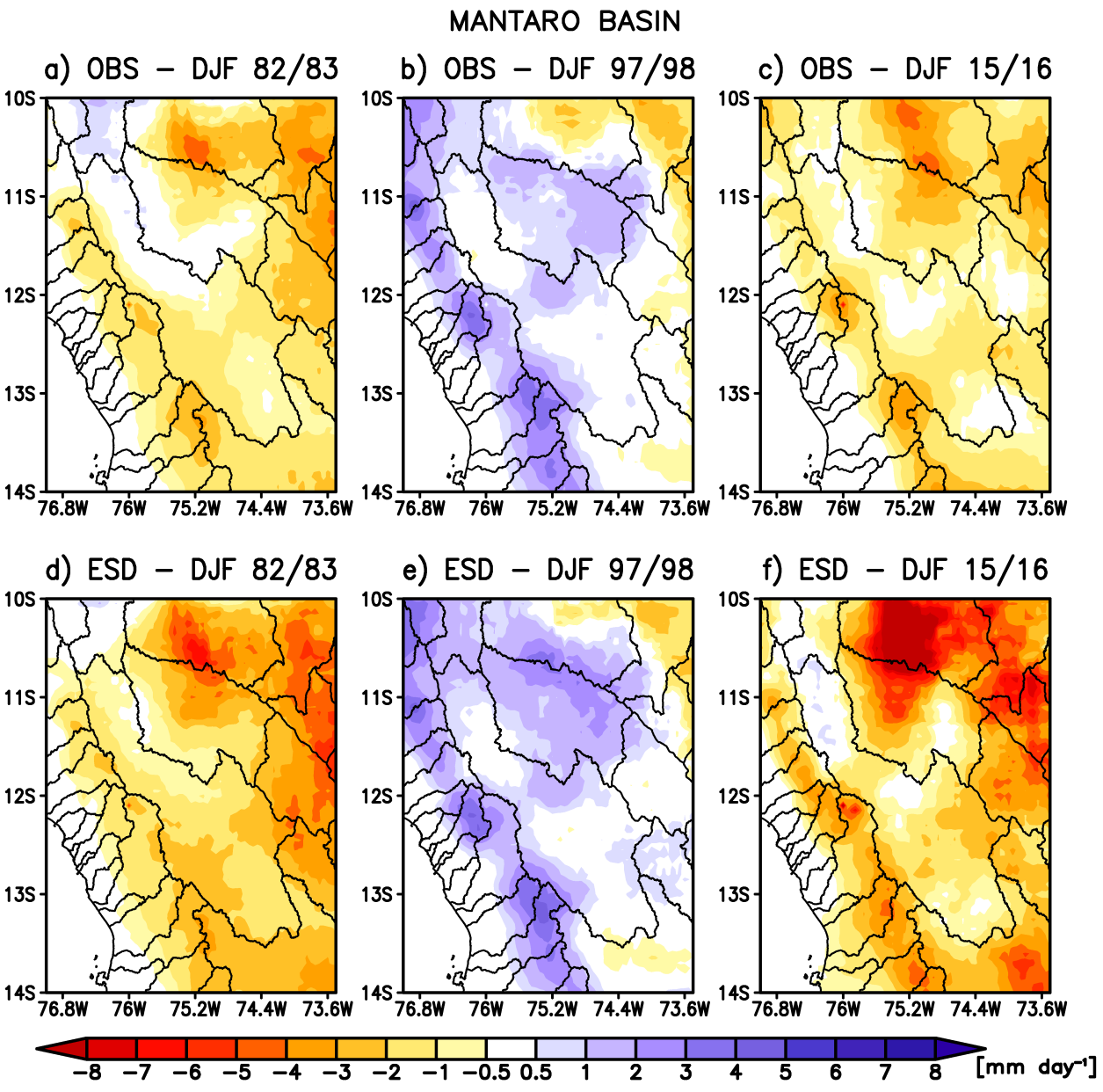

FIG. 13. As in Fig. 12, but over the MB. The PISCO v1.0 dataset was used in this analysis.

of the dry anomalies over the eastern part of Northeast Brazil. These latter results agree with the lack of skill of the ESD model over the southern Amazon basin and northeastern Brazil. Most of the Mantaro basin was anomalously wet in DJF 1997–98 (Fig. 13b), which is very well reproduced by the ESD model in terms of the spatial pattern (Fig. 13e).

In DJF 2015/16, rainfall was above average over northeastern Brazil and SESA (central and northern Argentina, Paraguay, Uruguay, and southernmost Brazil), while dry anomalies prevailed over the equatorial and western Amazon basin, and central Brazil (Fig. 12c). Figure 12f shows the predominance of model-estimated negative precipitation anomalies over the central and eastern equatorial Amazon basin while positive precipitation anomalies prevail over central and northern Argentina, SESA, Paraguay, and eastern Brazil. In general, the model overestimates the amplitude of both positive and negative precipitation anomalies. The Mantaro basin presents dry anomalies, except over the central and southernmost part of the MB, where weak wet anomalies ($<0.5\,\mathrm{mm\,day^{-1}}$) dominate (Fig. 13c). The largest dry anomalies are found along the Western Cordillera of the central Andes of Peru. Figure 13f illustrates that the ESD model reproduces the observed pattern of DJF precipitation anomalies over the entire MB well, but it overestimates the observed intensity of the wet and dry anomalies. Note here that the 2015/16 event provides a more stringent test for the model, because this event falls into the

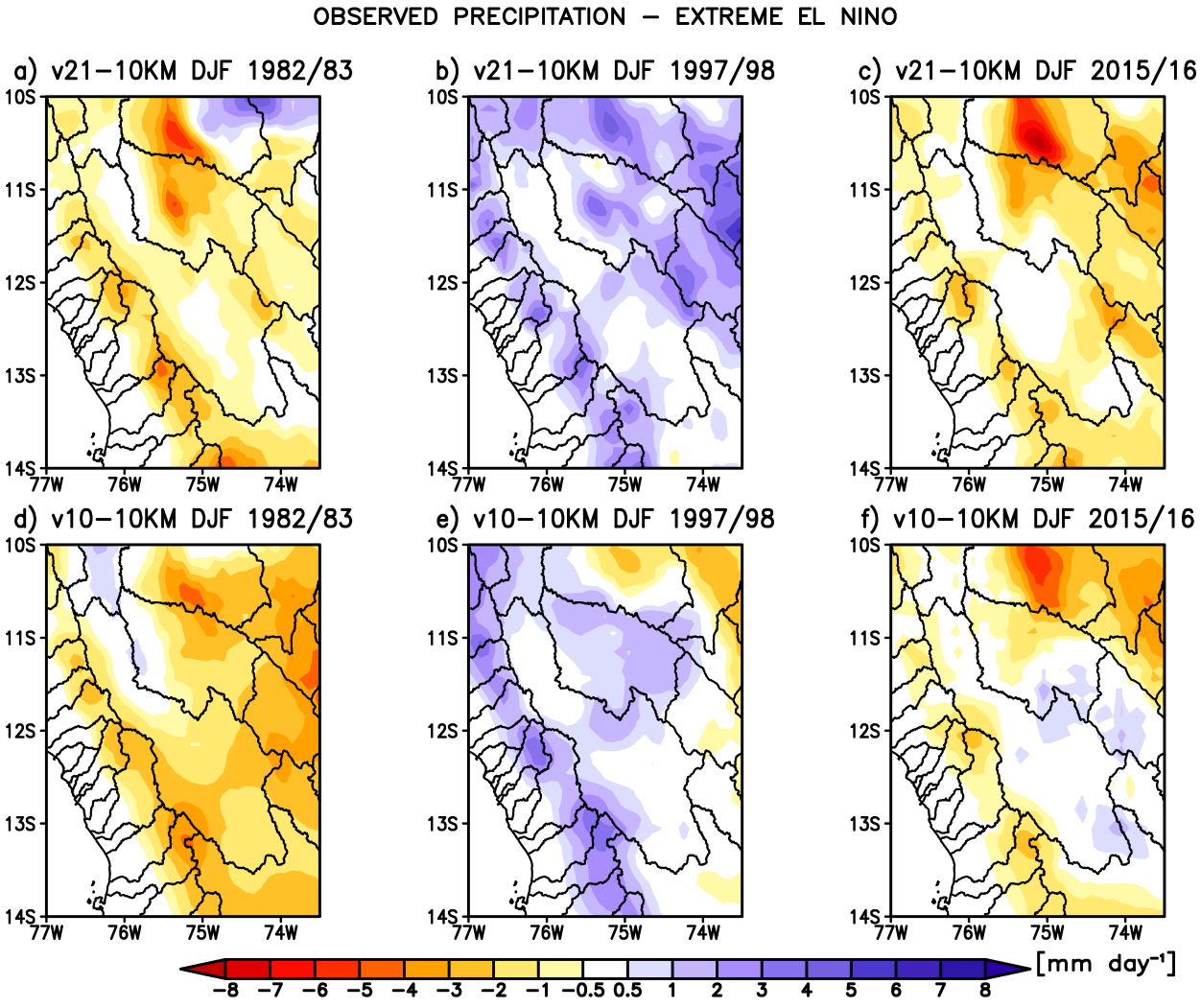

FIG. 14. DJF precipitation anomalies (mm day^{-1}) over the MB for the three extreme El Niño episodes: (left) 1982/83, (center) 1997/98, and (right) 2015/16 in (a)–(c) PISCO v2.1 and (d)–(f) PISCO v1.0. The PISCO v2.1 presents a horizontal resolution of 10 km. The PISCO v1.0 data were interpolated to 10 km.

validation period whereas the other two events (1982/83 and 1997/98) form part of the calibration dataset.

We repeated the same analysis using versions 1.0 and 2.1 of the PISCO data that have the same horizontal resolution of 10 km (Figs. 14 and 15). Figure 14 shows that both versions 1.0 and 2.1 of PISCO data present a similar pattern of DJF precipitation, although the PISCO v2.1 data show a positive precipitation bias in the ESD model over the northern part of the western Peruvian Cordillera in all three El Niño episodes (Figs. 15a–c).

The dry anomalies seen during El Niño events over the eastern equatorial Amazon (Fig. 16b) are caused by the interaction between an upper-level anomalous anticyclonic circulation and an upper-level Kelvin wave response associated with the southward displacement of the SACZ and the deep convection over the tropical Atlantic Ocean, respectively. This latter aspect is confirmed by the comparison of experiments Exp-2 (Figs. 16c,d) and ESD (Figs. 16e,f), which shows that the combination of the ENSO forcing, the SACZ forcing, and the Atlantic Ocean forcing creates the dry anomalies over the eastern equatorial Amazon basin in the ESD model (Figs. 16e,f), but not the dry anomalies over the Mantaro basin. Hence, the ENSO forcing is insufficient to fully explain the extreme 2015/16 dry anomalies over the eastern equatorial Amazon on its own (Antico and Diaz 2019), although climatologically dry anomalies as such are significant consequences of El Niño events (Dong et al. 2018). This study thereby confirms results by Jiménez-Muñoz et al. (2016) and Erfanian et al. (2017), who suggested that the two El Niño episodes in 1982/83 and 1997/98 caused the equatorial Amazon drought through the eastward displacement of the Walker circulation, while this latter mechanism cannot produce the equatorial Amazon drought observed during the extreme El Niño 2015/16. Moreover, Jiménez-Muñoz et al. (2021) recently found that neither ENSO forcing nor the anomalously warm

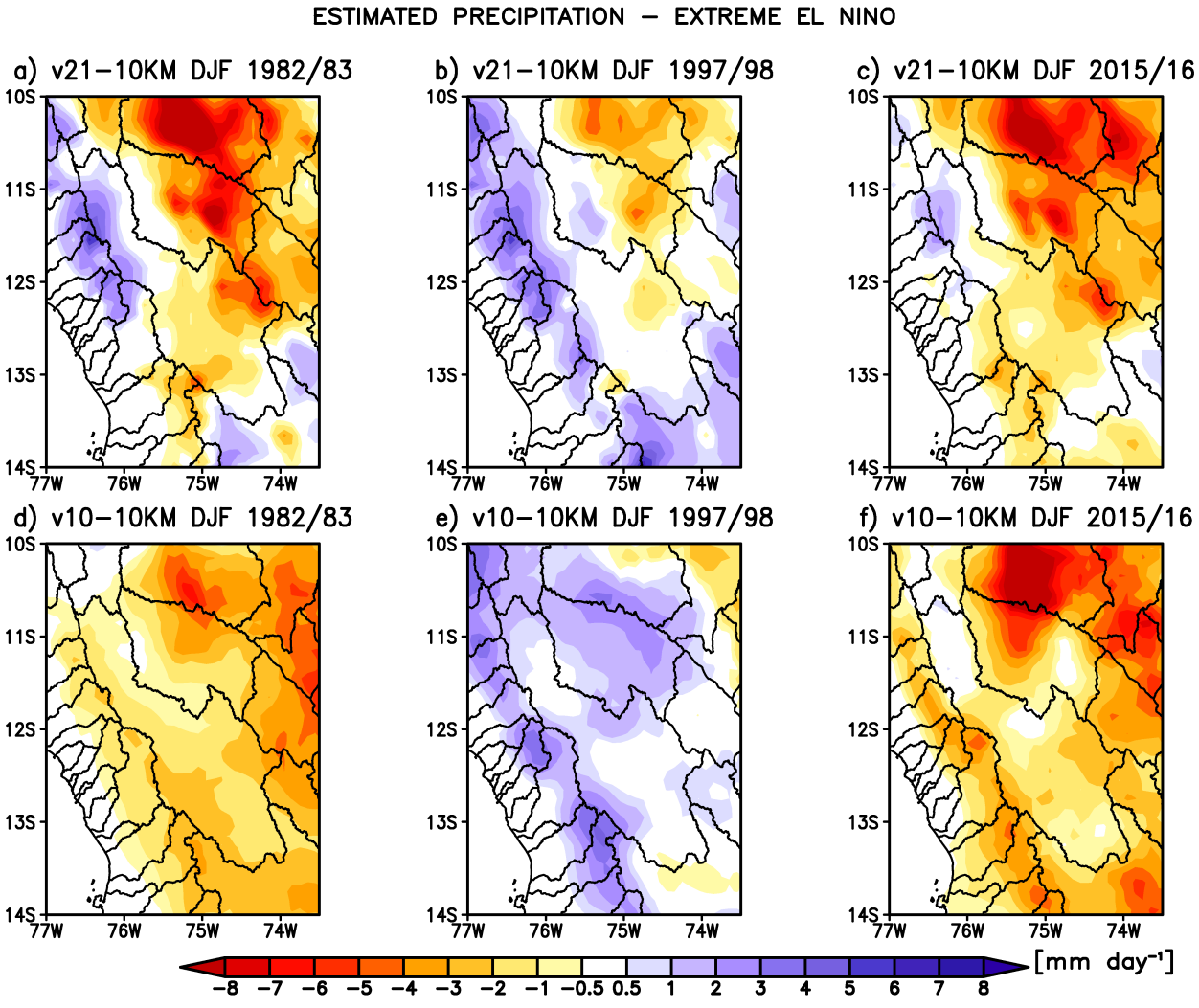

FIG. 15. As in Fig. 14, but estimated by the ESD model.

North Pacific Ocean can account for a complete description of the 2016 drought.

6. Conclusions

The main objective of this study was to provide an empirical–statistical downscaling model for precipitation over South America, with a focus on the central Peruvian Andes and the MB, using all forcings (C, E, latE, latW, ITCZc, ITCZe, ATL, and SACZ) during austral summer (December–February) for the 1982–2016 period.

The observed precipitation anomalies along the Western Cordillera of the central Peruvian Andes and eastern boundary of the MB present a statistically significant negative relationship with the zonal wind anomalies at 200 hPa ($r = -0.68$; $p < 0.05$) during austral summer on interannual time scales. This result agrees with previous studies about the relationship between upper-level zonal wind anomalies and precipitation in the central Andes during austral summer on interannual time scales (Vuille and Keimig 2004; Minvielle and Garreaud 2011; Segura et al. 2019) and even during the past millennium (Neukom et al. 2015).

The observational rain gauge stations and gridded precipitation (CPC_UNI and PISCO v1.0 datasets) products validate the atmospheric teleconnection between the SACZ and DJF precipitation over SA during austral summer, as was suggested in previous numerical studies (Chen et al. 1999; Barros et al. 2000; Barreiro et al. 2002). For instance, positive SACZ anomalies induce wet anomalies over central and northern Argentina and SESA (Uruguay, Paraguay, and northeastern Argentina) while dry anomalies result in Venezuela, the tropical Andes (Colombia, Ecuador, Peru, and northern Bolivia) and the equatorial Amazon basin during austral summer. Moreover, positive SACZ anomalies induce dry anomalies over the eastern boundary of the MB and along the Western Cordillera of the central Peruvian Andes, which presents the maximum dry anomalies. This anomalous DJF precipitation pattern over SA is associated with a weakening of the entire BH–NL system, for

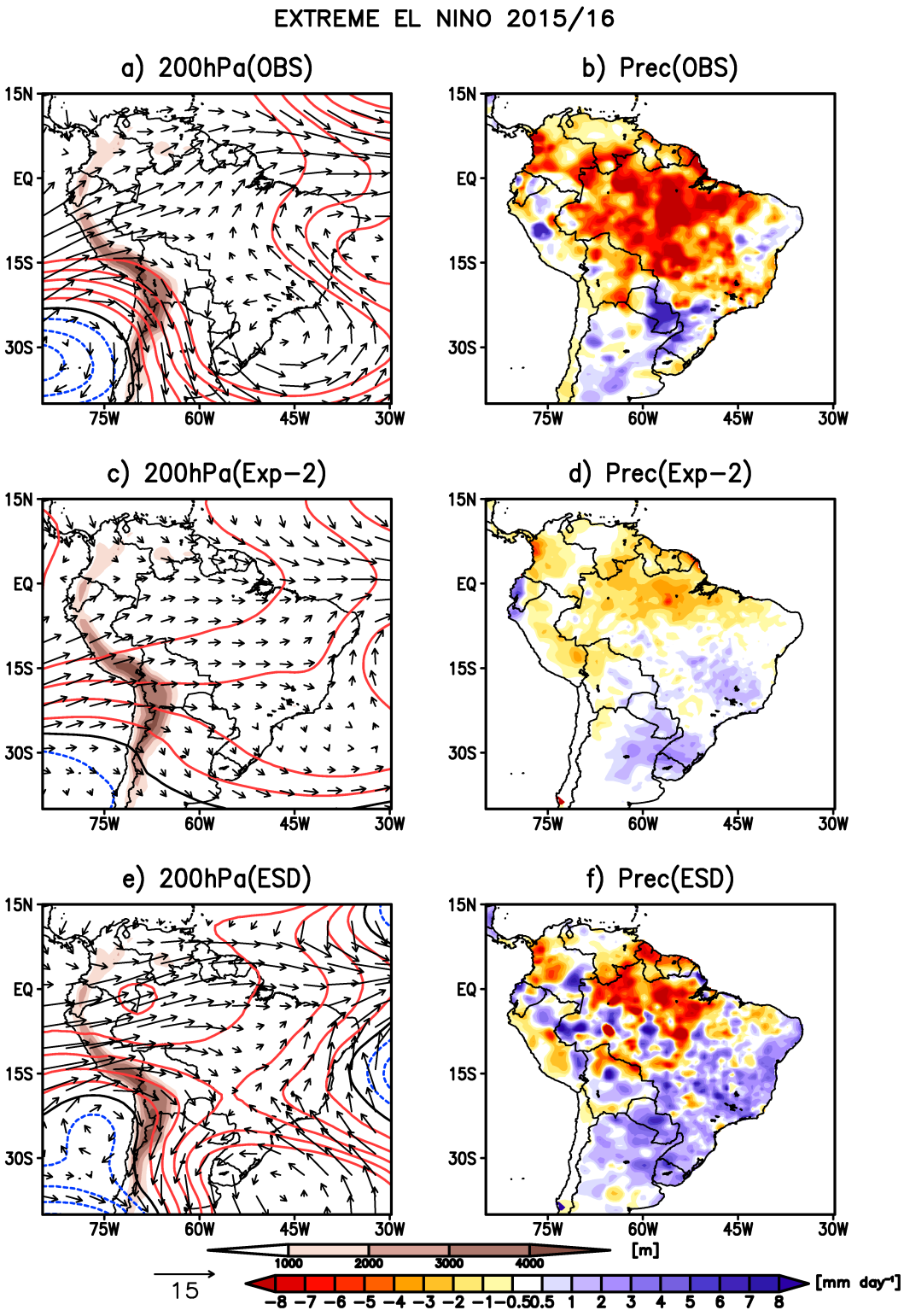

FIG. 16. Anomaly fields of (a),(c),(e) 200-hPa wind (m s^{-1}) and geopotential height (m) and (b),(d),(f) precipitation (mm day^{-1}) over South America during the extreme El Niño 2015/16 for (top) the observed fields, (middle) Exp-2, and (bottom) the ESD model. Experiment-2 includes some convection forcings (ENSO, SPCZ, ITCZ, and ATL). The ESD model includes all convection forcings (ENSO, SPCZ, ITCZ, ATL, and SACZ). ERA-Interim reanalysis and CPC_UNI datasets were used in this analysis. The contour interval of the geopotential height anomalies is 100 m. Brown shading represents the topographic elevation of the Andes.

example, 200-hPa westerly wind anomalies dominate over all of Peru, and an anticyclonic circulation is established over SESA at upper-tropospheric levels.

The ESD model reproduces the spatial distribution of DJF precipitation over South America quite well. The ESD model performs well when estimating the dry anomalies over the central and eastern equatorial Amazon and precipitation anomalies over the MB during the three extreme El Niño episodes (1982/83, 1997/98, and 2015/16). For instance, the ESD model corroborates the hypothesis that the interaction between the SACZ and the tropical Atlantic Ocean may be the main driver of the Amazon drought in 2015/16, in contrast to Amazon droughts in 1982/83 and 1997/98 that were associated with the eastward shift of the Pacific cell (Jiménez-Muñoz et al. 2016, 2021).

The addition of the equatorial Atlantic Ocean and SACZ forcings in the ESD model improves the estimation of DJF precipitation anomalies over the central Andes of Peru and the Peruvian Amazon when compared with an ESD model that only includes the ENSO forcing. The Pacific convective (SPCZ and ITCZ) forcing appears to partially explain the dry anomalies along the Eastern Cordillera of the central Andes of Peru, since the ESD models that only include ENSO, ATL, and SACZ forcings as predictors cannot reproduce the observed intensity of the dry anomalies over this region.

Despite these advances, the current study also documents several limitations in the ESD model. The main limitation to train and validate the ESD model is related to the lack of long observational time series, as well as the sparse observational network over regions of complex topography (e.g., Mantaro basin).

The ESD model's architecture presents deficiencies as well, especially over regions where local forcings are important, such as along the coasts of northern Peru and Ecuador. Here, the ESD model lacks predictors that include information on coastal SSTA to simulate the interaction of ocean and atmosphere associated with the coastal El Niño, which constitutes a local-scale phenomenon (Takahashi and Martínez 2019; Peng et al. 2019; Rodríguez-Morata et al. 2019). Similarly, over the central and southern Amazon basin, the ESD model could be further improved by including a predictor index of moisture flux convergence, which controls the interannual variability of precipitation over the central and southern Amazon basin (Misra et al. 2002).

Acknowledgments. The authors thank the PPR 068 "Reducción de vulnerabilidad y atención de emergencias por desastres" program. The authors also thank Dr. Takahashi for useful discussions during the initial part of this study. Moreover, the authors thank Ing. Prudencio for his help with the production of some figures. The authors also thank Dr. Lavado-Casimiro and his group (Cesar Aybar and Fiorella Vega) for providing the PISCO data. The authors also thank the project "MAGNET-IGP: Strengthening the research line in physics and microphysics of the atmosphere (Agreement 010-2017-FONDECYT)," financed by the Consejo Nacional de Ciencia y Tecnología (CONCYTEC), Peru. We are very grateful to three anonymous reviewers who provided us with valuable comments, which helped us to advance our results significantly and to improve the paper. Author M. Vuille was partially supported by NSF-PIRE (OISE-1743738) and NSF-P2C2 (AGS-1702439). This work was performed using computational resources, HPC-Linux-Cluster, from the Laboratorio de Dinámica de Fluidos Geofísicos Computacionales (http://scah.igp.gob.pe/laboratorios/dfgc) at the Instituto Geofísico del Perú (Grant 101-2014-FONDECYT).

REFERENCES

Antico, A., and H. F. Diaz, 2019: Why was the Paraná flood of 2016 weaker than that of 1998? *Int. J. Climatol.*, **40**, 604–609, https://doi.org/10.1002/joc.6204.

Aybar, C., C. Fernández, A. Huerta, W. Lavado, F. Vega, and O. Felipe-Obando, 2019: Construction of a high-resolution gridded rainfall dataset for Peru from 1981 to the present day. *Hydrol. Sci. J.*, **65**, 770–785, https://doi.org/10.1080/02626667.2019.1649411.

Barreiro, M., P. Chang, and R. Saravanan, 2002: Variability of the South Atlantic convergence zone simulated by an atmospheric general circulation model. *J. Climate*, **15**, 745–763, https://doi.org/10.1175/1520-0442(2002)015<0745:VOTSAC>2.0.CO;2.

Barros, V., M. Gonzales, B. Liebmann, and I. Camilloni, 2000: Influence of the South Atlantic convergence zone and South Atlantic sea surface temperature on interannual summer rainfall variability in southeastern South America. *Theor. Appl. Climatol.*, **67**, 123–133, https://doi.org/10.1007/s007040070002.

Beaton, R. H., and J. W. Tukey, 1974: The fitting of power series, meaning polynomials, illustrated on band-spectroscopic data. *Technometrics*, **16**, 147–185, https://doi.org/10.1080/00401706.1974.10489171.

Benestad, R. E., I. Hanssen-Bauer, and D. Chen, 2008: *Empirical–Statistical Downscaling*. World Scientific, 228 pp.

Chatterjee, S., and A. S. Hadi, 1986: Influential observations, high leverage points, and outliers in linear regression. *Stat. Sci.*, **1**, 379–393, https://doi.org/10.1214/ss/1177013622.

Chen, M., W. Shi, P. Xie, V. B. S. Silva, V. E. Kousky, R. W. Higgins, and J. E. Janowiak, 2008: Assessing objective techniques for gauge-based analyses of global daily precipitation. *J. Geophys. Res.*, **113**, D04110, https://doi.org/10.1029/2007JD009132.

Chen, T.-S., S.-P. Weng, and S. Schubert, 1999: Maintenance of austral summertime upper-tropospheric circulation over tropical South America: The Bolivian high–Nordeste low system. *J. Atmos. Sci.*, **56**, 2081–2100, https://doi.org/10.1175/1520-0469(1999)056<2081:MOASUT>2.0.CO;2.

Dee, D. P., and Coauthors, 2011: The ERA-Interim reanalysis: Configuration and performance of the data assimilation system. *Quart. J. Roy. Meteor. Soc.*, **137**, 553–597, https://doi.org/10.1002/qj.828.

Diack, C. A. T., 1999: A consistent nonparametric test of the convexity of regression based on the least squares splines. Eurandom Technical Worker Paper Rep. 99-001, 17 pp., http://alexandria.tue.nl/repository/books/521598.pdf.

Dong, B., A. Dai, M. Vuille, and O. E. Timm, 2018: Asymmetric modulation of ENSO teleconnections by the interdecadal Pacific oscillation. *J. Climate*, **31**, 7337–7361, https://doi.org/10.1175/JCLI-D-17-0663.1.

DuMouchel, W. H., and F. L. O'Brien, 1989: Integrating a robust option into a multiple regression computing environment. *Computer Science and Statistics/Proc. 21st Symp. on the Interface*, Alexandria, VA, American Statistical Association, 297–302.

Echevin, V., F. Colas, D. Espinoza-Morriberon, L. Vasquez, T. Anculle, and D. Gutierrez, 2018: Forcings and evolution of

the 2017 coastal El Niño off northern Peru and Ecuador. *Front. Mar. Sci.*, **5**, 367, https://doi.org/10.3389/FMARS.2018.00367.

Emerton, R., H. L. Cloke, E. M. Stephens, E. Zsoter, S. J. Woolnough, and F. Pappenberger, 2017: Complex picture for likelihood of ENSO-driven flood hazard. *Nat. Commun.*, **8**, 14796, https://doi.org/10.1038/ncomms14796.

Enfield, D. B., 1996: Relationships of inter-American rainfall to tropical Atlantic and Pacific SST variability. *Geophys. Res. Lett.*, **23**, 3305–3308, https://doi.org/10.1029/96GL03231.

Erfanian, A., G. Wang, and L. Fomenko, 2017: Unprecedented drought over tropical South America in 2016: Significantly under-predicted by tropical SST. *Sci. Rep.*, **7**, 5811, https://doi.org/10.1038/s41598-017-05373-2.

Florax, R., and H. Folmer, 1992: Specification and estimation of spatial linear regression models: Monte Carlo evaluation of pre-test estimators. *Reg. Sci. Urban Econ.*, **22**, 405–432, https://doi.org/10.1016/0166-0462(92)90037-2.

French, A., and R. Mechler, 2017: Managing El Niño risks under uncertainty in Peru: Learning from the past for a more disaster-resilient future. International Institute for Applied Systems Analysis Rep., 39 pp., http://pure.iiasa.ac.at/id/eprint/14849/1/French_Mechler_2017_El%20Ni%C3%B1o_Risk_Peru_Report.pdf.

Garreaud, R. D., M. Vuille, R. H. Compagnucci, and J. Marengo, 2009: Present-day South American climate. *Palaeogeogr. Palaeoclimatol. Palaeoecol.*, **281**, 180–195, https://doi.org/10.1016/j.palaeo.2007.10.032.

Hu, Z.-Z., B. Huang, J. Zhu, A. Kumar, and M. J. McPhaden, 2019: On the variety of coastal El Niño events. *Climate Dyn.*, **52**, 7537–7552, https://doi.org/10.1007/s00382-018-4290-4.

Huggel, C., A. Raissig, M. Rohrer, G. Romero, A. Diaz, and N. Salzmann, 2015: How useful and reliable are disaster databases in the context of climate and global change? A comparative case study analysis in Peru. *Nat. Hazards Earth Syst. Sci.*, **15**, 475–485, https://doi.org/10.5194/nhess-15-475-2015.

Instituto Geofísico del Peru, 2005: Vulnerabilidad actual y futura ante el cambio climático y medidas de adaptación en la cuenca del río Mantaro (Current and future vulnerability to climate change and adaptation measures in the Mantaro River basin). CONAM Publ., 107 pp., http://www.met.igp.gob.pe/publicaciones/2000_2007/Vulnerabilidad_actual_futura.pdf.

Jauregui, Y. R., and K. Takahashi, 2018: Simple physical-empirical model of the precipitation distribution in the tropical oceans and the effects of climate change. *Climate Dyn.*, **50**, 2217–2237, https://doi.org/10.1007/s00382-017-3745-3.

Jiang, X., B. Zou, H. Feng, J. Tang, Y. Tu, and X. Zhao, 2019: Spatial distribution mapping of Hg contamination in subclasses agricultural soils using GISS enhanced multiple linear regression. *J. Geochem. Explor.*, **196**, 1–7, https://doi.org/10.1016/j.gexplo.2018.10.002.

Jiménez-Muñoz, J. C., C. Mattar, J. Barichivich, A. Santamaría-Artigas, K. Takahashi, Y. Malhi, J. A. Sobrino, and G. Van der Schrier, 2016: Record-breaking warming and extreme drought in the Amazon rainforest during the course of El Niño 2015–2016. *Sci. Rep.*, **6**, 33130, https://doi.org/10.1038/srep33130.

——, J. A. Marengo, L. M. Alves, J. C. Sulca, K. Takahashi, S. Ferret, and M. Collins, 2021: The role of ENSO flavours and TNA on recent droughts over Amazon forests and the Northeast Brazil region. *Int. J. Climatol.*, https://doi.org/10.1002/joc.6453, in press.

Kodama, Y., 1992: Large-scale common features of subtropical precipitation zones (the baiu frontal zone, the SPCZ, and the SACZ) Part I: Characteristics of subtropical frontal zones. *J. Meteor. Soc. Japan*, **70**, 813–836, https://doi.org/10.2151/jmsj1965.70.4_813.

Lavado, W., C. Fernández, F. Vega, T. Caycho, S. Endara, A. Huerta, and O. F. Obando, 2016: PISCO: Peruvian interpolated data of the SENAMHI's climatological and hydrological observations. Precipitación v1.0. Servicio Nacional de Meteorología e Hidrología Doc., 5 pp.

Lenters, J. D., and K. H. Cook, 1997: On the origin of the Bolivian high and related circulation features of the South American climate. *J. Atmos. Sci.*, **54**, 656–678, https://doi.org/10.1175/1520-0469(1997)054<0656:OTOOTB>2.0.CO;2.

L'Heureux, M. L., and Coauthors, 2016: Observing and predicting the 2015/16 El Niño. *Bull. Amer. Meteor. Soc.*, **98**, 1363–1382, https://doi.org/10.1175/BAMS-D-16-0009.1.

Liebmann, B., and C. A. Smith, 1996: Description of a complete (interpolated) outgoing longwave radiation dataset. *Bull. Amer. Meteor. Soc.*, **77**, 1275–1277, https://doi.org/10.1175/1520-0477-77.6.1274.

——, G. N. Kiladis, J. Marengo, T. Ambrizzi, and J. D. Glick, 1999: Submonthly convective variability over South America and the South Atlantic convergence zone. *J. Climate*, **12**, 1877–1891, https://doi.org/10.1175/1520-0442(1999)012<1877:SCVOSA>2.0.CO;2.

Ma, H.-Y., X. Ji, J. D. Neelin, and C. R. Mechoso, 2011: Mechanisms for precipitation variability of the eastern Brazil/SACZ convective margin. *J. Climate*, **24**, 3445–3456, https://doi.org/10.1175/2011JCLI4070.1.

Marengo, J. A., B. Liebmann, V. E. Kousky, N. P. Filizola, and I. C. Wainer, 2001: Onset and end of the rainy season in the Brazilian Amazon basin. *J. Climate*, **14**, 833–852, https://doi.org/10.1175/1520-0442(2001)014<0833:OAEOTR>2.0.CO;2.

——, and Coauthors, 2012: Recent developments on the South American monsoon system. *Int. J. Climatol.*, **32**, 1–21, https://doi.org/10.1002/joc.2254.

Minvielle, M., and R. D. Garreaud, 2011: Projecting rainfall changes over the South American Altiplano. *J. Climate*, **24**, 4577–4583, https://doi.org/10.1175/JCLI-D-11-00051.1.

Misra, V., 2004: An evaluation of the predictability of austral summer season precipitation over South America. *J. Climate*, **17**, 1161–1175, https://doi.org/10.1175/1520-0442(2004)017<1161:AEOTPO>2.0.CO;2.

——, P. A. Dirmeyer, B. P. Kirtman, H.-M. H. Juang, and M. Kanamitsu, 2002: Regional simulation of interannual variability over South America. *J. Geophys. Res.*, **107**, 8036, https://doi.org/10.1029/2001JD900216.

Montini, T. L., Ch. Jones, and L. M. V. Carvalho, 2019: The South American low-level jet: A new climatology, variability, and changes. *J. Geophys. Res. Atmos.*, **124**, 1200–1218, https://doi.org/10.1029/2018JD029634.

Neukom, R., M. Rohrer, P. Calanca, N. Salzmann, C. Huggel, and D. Acuña, 2015: Facing unprecedented drying of the central Andes? Precipitation variability over the period AD 1000–2100. *Environ. Res. Lett.*, **10**, 084017, https://doi.org/10.1088/1748-9326/10/8/084017.

Peng, Q., S.-P. Xie, D. Wang, X.-T. Zheng, and H. Zhang, 2019: Coupled ocean-atmosphere dynamics of the 2017 extreme coastal El Niño. *Nat. Commun.*, **10**, 298, https://doi.org/10.1038/s41467-018-08258-8.

Raia, A., and I. F. A. Cavalcanti, 2008: The life cycle of the South American monsoon system. *J. Climate*, **21**, 6227–6246, https://doi.org/10.1175/2008JCLI2249.1.

Rayner, N. A., D. E. Parker, E. B. Horton, C. K. Folland, L. V. Alexander, D. P. Rowell, E. C. Kent, and A. Kaplan, 2003: Global

analyses of sea surface temperature, sea ice, and night marine air temperature since the late nineteenth century. *J. Geophys. Res.*, **108**, 4407, https://doi.org/10.1029/2002JD002670.

Robertson, A. W., and C. R. Mechoso, 2000: Interannual and interdecadal variability of the South Atlantic convergence zone. *Mon. Wea. Rev.*, **128**, 2947–2957, https://doi.org/10.1175/1520-0493(2000)128<2947:IAIVOT>2.0.CO;2.

Rodríguez-Morata, C., J. A. Ballesteros-Canovas, M. Rohrer, J.-C. Espinoza, M. Beniston, and M. Stoffel, 2018: Linking atmospheric circulation patterns with hydro-geomorphic disasters in Peru. *Int. J. Climatol.*, **38**, 3388–3404, https://doi.org/10.1002/joc.5507.

——, H. F. Díaz, J. A. Ballesteros-Canovas, M. Rohrer, and M. Stoffel, 2019: The anomalous 2017 coastal El Niño event in Peru. *Climate Dyn.*, **52**, 5605–5622, https://doi.org/10.1007/s00382-018-4466-y.

Sangati, M., and M. Borga, 2009: Influence of rainfall spatial resolution on flash flood modelling. *Nat. Hazards Earth Syst. Sci.*, **9**, 575–584, https://doi.org/10.5194/nhess-9-575-2009.

Segura, H., C. Junquas, J.-C. Espinoza, M. Vuille, Y. R. Jauregui, A. Rabatel, T. Condom, and T. Lebel, 2019: New insights into the rainfall variability in the tropical Andes on seasonal and interannual time scales. *Climate Dyn.*, **53**, 405–426, https://doi.org/10.1007/s00382-018-4590-8.

SENAMHI, 2014: El fenómeno de El Niño en el Perú (The El Niño phenomenon in Peru). Servicio Nacional de Meteorología e Hidrología Doc., 33 pp., http://www.minam.gob.pe/wp-content/uploads/2014/07/Dossier-El-Ni%C3%B1o-Final_web.pdf.

——, 2019: Caracterización espacio temporal de la sequía en los departamentos altoandinos del Perú (1981–2018) [Spatial-temporal characterization of the drought in the high Andean departments of Peru]. Servicio Nacional de Meteorología e Hidrología Doc., 29 pp., https://www.senamhi.gob.pe/load/file/01401SENA-78.pdf.

Sharifi, E., B. Saghafian, and R. Steinacker, 2019: Downscaling satellite precipitation estimates with multiple linear regression, artificial neural networks, and spline interpolation techniques. *J. Geophys. Res. Atmos.*, **124**, 789–805, https://doi.org/10.1029/2018JD028795.

Silva Dias, P. L., W. H. Schubert, and M. De Maria, 1983: Large-scale response of the tropical atmosphere to transient convection. *J. Atmos. Sci.*, **40**, 2689–2707, https://doi.org/10.1175/1520-0469(1983)040<2689:LSROTT>2.0.CO;2.

Sulca, J., M. Vuille, Y. Silva, and K. Takahashi, 2016: Teleconnections between the central Peruvian Andes and Northeast Brazil during extreme rainfall events in austral summer. *J. Hydrometeor.*, **17**, 499–515, https://doi.org/10.1175/JHM-D-15-0034.1.

——, K. Takahashi, J.-C. Espinoza, M. Vuille, and W. Lavado-Casimiro, 2018: Impacts of different ENSO flavors and tropical Pacific convection variability (ITCZ, SPCZ) on austral summer rainfall in South America, with a focus on Peru. *Int. J. Climatol.*, **38**, 420–435, https://doi.org/10.1002/joc.5185.

Takahashi, K., and A. Martínez, 2019: The very strong coastal El Niño in 1925 in the far-eastern Pacific. *Climate Dyn.*, **52**, 7389–7415, https://doi.org/10.1007/s00382-017-3702-1.

——, A. Montecinos, K. Goubanova, and B. Dewitte, 2011: ENSO regimes: Reinterpreting the canonical and Modoki El Niño. *Geophys. Res. Lett.*, **38**, L10704, https://doi.org/10.1029/2011GL047364.

Vargas, P., 2009: El cambio climático y sus efectos en el Perú (Climate change and its effects in Peru). Banco Central de Reserva del Perú, Working Papers Series D.T. 2009-14, 59 pp.

Vincent, E. M., M. Lengaigne, C. E. Menkes, N. C. Jourdain, P. Marchesiello, and G. Madec, 2011: Interannual variability of the South Pacific convergence zone and implications for tropical cyclone genesis. *Climate Dyn.*, **36**, 1881–1896, https://doi.org/10.1007/s00382-009-0716-3.

Vuille, M., and F. Keimig, 2004: Interannual variability of summertime convective cloudiness and precipitation in the central Andes derived from ISCCP-B3 data. *J. Climate*, **17**, 3334–3348, https://doi.org/10.1175/1520-0442(2004)017<3334:IVOSCC>2.0.CO;2.

——, R. S. Bradley, and F. Keimig, 2000: Interannual climate variability in the central Andes and its relation to tropical Pacific and Atlantic forcing. *J. Geophys. Res.*, **105**, 12 447–12 460, https://doi.org/10.1029/2000JD900134.

——, G. Kaser, and I. Juen, 2008: Glacier mass balance variability in the Cordillera Blanca, Peru and its relationship with climate and the large-scale circulation. *Global Planet. Change*, **62**, 14–28, https://doi.org/10.1016/j.gloplacha.2007.11.003.

Wilks, D. S., 2011: *Statistical Methods in the Atmospheric Sciences*. 3rd ed. Elsevier, 676 pp.

Wu, S., M. Notaro, S. Vavrus, E. Mortensen, R. Montgomery, J. de Piérola, and P. Block, 2018: Efficacy of tendency and linear inverse models to predict southern Peru's rainy season precipitation. *Int. J. Climatol.*, **38**, 2590–2604, https://doi.org/10.1002/joc.5442.

Yarleque, C., M. Vuille, D. R. Hardy, A. Posadas, and R. Quiroz, 2016: Multi-scale assessment of spatial precipitation variability over complex mountain terrain using a high-resolution spatiotemporal wavelet reconstruction method. *J. Geophys. Res. Atmos.*, **121**, 12 198–12 216, https://doi.org/10.1002/2016JD025647.

Zhou, J., and K. M. Lau, 1998: Does a monsoon climate exist over South America? *J. Climate*, **11**, 1020–1041, https://doi.org/10.1175/1520-0442(1998)011<1020:DAMCEO>2.0.CO;2.